NEVIS - 88

NEVIS CYCLOTRON LABORATORY

COLUMBIA UNIVERSITY
PHYSICS DEPARTMENT
Irvington-on-Hudson,
New York

π^- SCATTERING FROM COMPLEX NUCLEI

R. M. EDELSTEIN

Joint ONR - AEC Program
Office of Naval Research Contract
Contract N6-ori-110 Task No. 1
AEC Contract AT(30-1)-1932

R - 259
CU - 190
Nevis - 88

Nevis Cyclotron Laboratory
Columbia University
Physics Department
Irvington-on-Hudson,
New York

π^- SCATTERING FROM COMPLEX NUCLEI

R. M. Edelstein

Submitted in partial fulfillment
of the requirements for the degree
of Doctor of Philosophy in the Faculty
of Pure Science, Columbia University
May, 1960

Joint ONR-AEC Program
Office of Naval Research Contract
Contract N6-ori-110-Task No. 1
AEC Contract AT(30-1)-1932

π^- Scattering From Complex Nuclei*

R. M. EDELSTEIN+

Columbia University, New York, New York

---

* This research is supported by the United States Atomic Energy Commission and the Office of Naval Research.

+ Submitted in partial fulfillment of the requirements for the degree of Doctor of Philosophy in the Faculty of Pure Science, Columbia University.

ABSTRACT

Differential cross sections were measured for π^- -carbon scattering at 69.5 Mev and 87.5 Mev and π^- -oxygen scattering at 87.5 Mev from 20^o to 125^o extending the technique of Baker, Rainwater, and Williams[1]. Elastic and 5 and 10 Mev inelastic cross sections were obtained. The energy resolution was sufficient to measure pure elastic cross sections. The modified Kisslinger optical model equation was used to fit the elastic cross section data. A χ^2 analysis for the 69.5 Mev carbon data gave a nuclear radius parameter, $r_o = 1.05 \pm 0.03$ fermis and a fall-off parameter, $t = 1.16 \pm 0.07$ fermis. These parameters give good fits to the other data as well. An energy dependence in the strength parameters for carbon is observed in qualitative agreement with prediction. A modification to the equation by Kroll does not give as close a fit to the data.

I. INTRODUCTION

Measurements have been made, with the use of scintillation counters, of the angular distributions of π^- mesons scattered from carbon at 69.5 Mev and 87.5 Mev and from oxygen at 87.5 Mev. The experimental work is an extension of that of Baker, Rainwater, and Williams[1] (BRW), in which the scattering of 80 Mev π^- mesons from Li, C, Al, and Cu was measured. In their experiment, scattered pion energy was determined from the range of pions stopped in a counter. This technique afforded considerable improvement in energy resolution over that obtained previously with counters[2-4] and cloud chambers[5-7]. The present experiment employed four such counters in succession, the "multicounter", to increase the data taking rate. The energy resolution in either experiment was sufficient to separate out pure elastic scattering from all inelastic scattering for carbon and oxygen. In the case of lithium, BRW employ the electron[8] and proton[9] scattering data to argue that the contribution of scattering from the first excited state to the measured elastic scattering is small. No other levels contribute.

Recent experiments have been performed by Kane[10], π^+-carbon scattering at 31.5 Mev; and Fujii[11], 150 Mev π^- scattering from C, Al, Cu, and Pb. Kane measured total pion energy by means of pulse height in a scintillation counter with an (absolute) energy resolution comparable to our own and observed backward (105° to 145°) elastic scattering cross sections of approximately 7 mb/ster. Fujii measured quasi-elastic scattering into a 15 Mev interval by means of total

energy determination in a Cerenkov counter and observed for carbon $\lesssim$ 1 mb/ster elastic scattering for $\theta \gtrsim 70^{o}$. This is significantly less scattering at large angles than we observe at 70-90 Mev; namely 2-5 mb/ster. The difference may well be due to the energy dependence of the π-nucleus interaction.

Baker, Byfield and Rainwater[12] (BBR) have fit optical model calculations to the data of BRW. The optical potential used was a modification of the one of Kisslinger[13]. It removes an obviously non-physical divergence in the unmodified form. The potential includes a term in the gradient of the nuclear density which arises from the important p wave contribution to the elemental π-nucleon scattering in the nucleus. Hence, the predictions are particularly sensitive to the nuclear edge thickness. The model gives good fits to the data at all angles and for nuclear radii consistent with the results of electron scattering[14]. The IBM 650 program of BBR has been used to fit the data of this experiment.

Kroll[15] has derived a modification of the Kisslinger theory which attempts to distinguish properly between the average and effective meson fields in the vicinity of a nucleon as is done in the Lorentz-Lorenz classical theory for electromagnetic waves in matter.

The mathematical form of his potential is intermediate between the unmodified form and the form of BBR. Considerable attempts have been made to fit Kroll's equation to the present data and the 80 Mev carbon data of BRW with less success than is afforded by the modified Kisslinger equation.

These models are discussed in Sections V and VI.

II. EXPERIMENTAL ARRANGEMENT

A. Detection Apparatus

The π^- meson beam used in this experiment was produced by the 380 Mev Nevis Synchrocyclotron. The mesons were focused and deflected into the detection apparatus by means of a series of magnetic lenses as indicated in Fig. 1.

The detection apparatus was laid out as shown in Fig. 2. Counter dimensions are listed in Table I. All counters were plastic scintillators and each was viewed by two RCA 1P21 photomultiplier tubes whose outputs were added. Counters 1, 2, and 3 make up the incoming beam telescope. Counter 3, which was 3/4" x 3", determined the target size used. The angular spread and the intensity of the part of the beam used were dependent on the position of counter 1 relative to counters 2 and 3. A compromise position, which gained considerable intensity without losing much angular resolution, was obtained with D_1 = 25". The carbon target used was 0.500 inches thick, the distance for a 5 Mev loss of energy by an 80 Mev pion by ionization. The oxygen target was a container of water with thickness 0.750 inches, the distance for a 5 Mev loss in water. The container was a light aluminum frame with 0.003 inch aluminum windows. 3/8 inch thick slabs of Styrofoam were glued to the windows to maintain uniform target thickness. Thus, the total thickness of material in the beam was 5% by weight of the target thickness. The hydrogen contamination to the elastic scattering was negligible (to be discussed in Section III). The remaining counters and absorbers formed the scattered beam telescope. Counters 4 and 5 detected pions of all energies scattered

through angle θ. Counter 5 defined the solid angle and the linear angle subtended by the scattered beam telescope. The distance D_5 was varied from 40 in. at small values of θ to 12 in. at large angles - all other distances in the scattered beam telescope remained fixed - to obtain maximum counting rate consistent with good angular resolution. The copper absorber slowed the pions so that most stopped in the "multicounter", counters 6 to 10, where pion energy was measured. The shield prevented all pions scattered in counter 3 from reaching the multicounter, except for $\theta \leq 30^{o}$ where it could be only partially effective.

The scattering stand used was the one described in BRW. The scattered beam telescope was mounted on an arm which rotated in a vertical plane. The absorber was mounted on a four positioned rotating wheel. The target was always kept in a transmission type geometry and rotated as the arm did to maintain $\phi = \frac{1}{2}\theta$. By this means, all π's scattered through θ traversed the same distance in the target thus maintaining energy resolution. The use of a transmission type geometry for the target prevents measurements for $\theta \gtrsim 125^{o}$. The scattering arm and the absorber wheel were operated remotely from the data recording site along with the target in-out control.

The multicounter - counters 6,7,8,9, and 10, and the copper shims between them - was used to measure simultaneously four points on the differential range curve of the scattered beam by counting stoppings in counters 6,7,8, and 9. It was set up as follows: In the straight ahead beam with the target

out, the absorber thickness, T, was adjusted so that the rate in counter 9 was maximized. This was done by adjusting T such that if R(T) is the rate for T, then R(T + 1/8 in.) = R(T - 1/8 in.) $\approx$ 0.4 R(T). We say that the beam was "centered" on counter 9. The shim and counter thicknesses were such that an increase in T by an amount equivalent to a 5, 10, or 15 Mev loss of energy by an incident π would center the beam on counter 8, 7, or 6, respectively. The stopping power of a shim was $\sim$ 2/3 the stopping power of a scintillator. As discussed below, the portion of the scattered beam which was detected was considered in the analysis to consist of 4 beams whose mean energies upon leaving the target were the elastic energy E_{el}; E_{el}-5; E_{el}-10; and E_{el}-15 Mev. Because of the way the multicounter was set up, these 4 beams were always centered respectively on counters 9,8,7, and 6. Each of these beams contributed counts to each of the counters because of the non-zero energy resolution of the system. Therefore, the efficiency of the counters was calibrated in the straight ahead beam for 4 different absorber thicknesses corresponding to the 4 beams. That is, the thicknesses were such that the straight ahead beam was centered in turn on each counter. Changing the absorber thickness is essentially equivalent to changing the mean energy of the incident beam without changing the energy distribution about the mean or the spatial distribution. Fig. 3A shows the response of the multicounter to a beam centered on counter 9 (Curve I) and on counter 6 (Curve II). The counting rate is in relative units, the counters having been adjusted for equal peak efficiencies.

From these curves it is seen that the measured energy spread is $\pm$ 4 Mev. This includes both the inherent spread of the beam as well as the spread introduced by the measuring process.

An alternate approach is to plot the range curve in a given counter for varying absorber thickness. Fig. 3B shows such a range curve for counter 9 with a beam energy of 72 Mev at the exit of counter 3. The overall energy spread measured in this way is also 8 Mev for either energy beam. Several additional points were taken to show the small relative efficiency in the tails of the distribution.

A stopped pion in a given counter was identified both by the extra large light pulse it produced and by the absence of a pulse in the following counter. A stopped pion produces a large light pulse because of its high specific ionization and because of the energy released in the star it produces. Anticoincidences 6-7', 7-8', 8-9', and 9-10' were made at the multicounter in the addition circuits shown in Fig. 4. The attenuated anode pulse (coincidence) of a counter was added to the pulse from the last dynode of the following counter (anticoincidence). In order that only large light pulses be detected, the coincidence circuits involving the multicounter pulses were operated on the knee of the high voltage plateau. To meet the stringent stability requirements, a well-regulated high voltage supply was used for the multicounter - stable to within 0.3 volt at 1400 volts - which together with the rest of the stable electronics proved very adequate. The multicounter was calibrated every 24 hours

and the drift was not sufficient to change the calculated cross sections by a statistically significant amount.

The contributions to the overall energy spread from the measuring process include range straggling, stars produced in flight, large angle scattering in the multicounter, and the energy interval corresponding to each counter. The tight geometry after counter 5 and the graduated sizes of counters 6 to 10, tended to minimize the effect of the large angle scattering; the other effects were necessarily present. At any event, the calibration of the multicounter, which measured the overall effective spread, is all that is required in order to reduce the raw data. The individual contributions to the final spread need not be known since these were present both in the calibration and in the data taking runs. Most important, the overall spread is small enough to make feasible the separation of the elastic from the inelastic scattering for carbon and oxygen.

B. Electronics

The block diagram of the electronics layout is shown in Fig. 5. The coincidence circuits were all Garwin type. Each counter pulse was amplified by a Hewlett-Packard amplifier, type 460A, which fed the fast coincidence circuits. The latter circuitry was all in the experimental area. It was necessary only to clip the counter pulses of high rate, counters 1,2, and 3. The 1-2-3 coincidence then had a resolving time of 6 mμsec. Its accidental rate at the maximum coincidence rate of 11,000 counts/sec was 1%. A 1-2-3-4-5 coincidence was made largely for use as a monitor. Coinci-

dences with multicounter pulses were 4-5-6-7', 4-5-7-8', 4-5-8-9', 4-5-9-10'. The resolving time for the latter 5 coincidences was 15 mμsec. The accidental rate in the multicounter coincidences was nil for $\theta \geq 35^{o}$. However, it was found that the singles and coincidence rates in the scattered beam telescope were increased at small θ because these counters then intercepted part of the raw beam. The beam intensity was reduced at these angles so as to make the accidentals rate negligible.

The pulses from these 6 coincidence circuits were sent to the laboratory building to the EFP60 discriminator and pulse shaping circuits. See Fig. 6. The stability of these circuits was the prime reason for the stability of the system. The control grid (discriminator) voltage to the EFP60 was stabilized by the cathode follower feed back loop. The shaped pulse width was 80 mμsec and the dead time between pulses was 20 mμsec. These times, as well as the pulse height, remained essentially the same up to rates of 2×10^{6} pulses/sec. Four slow coincidences were made after the EFP60 circuits: 123-12345-4567', 123-12345-4578', etc. Each of the 4 outputs was sent to two 200 kilocycle scalers in parallel as a precaution against scaler breakdown. The shaped 1-2-3 and 1-2-3-4-5 pulses were also sent to fast amplifiers and then to 10 megacycle Hewlett-Packard scalers which in turn went to 200 kilocycle scalers. The only significant dead time in the system was introduced in the 1-2-3 coincidence. The dead time correction was found to be 6% at a 1-2-3 rate of 10,000 counts/sec and to vary linearly

with rate. A suitable correction is made to the cross sections.

C. Beams

The meson beam was focused by the following means. See Fig. 1. The vertical source size for π mesons at the cyclotron target is 0.8 in. as determined by a radiogram of the cyclotron target. The cyclotron fringing field produces vertical focusing of the emerging beam so that vertically there is an apparent source which is $\sim$ 2 in. high at the point labeled V.S. Horizontally the beam is less coherent so that the air core quadrupole, Q_1, which focuses vertically to increase beam intensity, does not act to decrease intensity by its horizontal defocusing action. The bending magnet, B, was shaped to focus vertically but not horizontally. There was then a vertical image at V.I. The quadrupole pair, Q_2 and Q_3, were horizontally and vertically focusing respectively. The horizontal source for the quadrupole pair may be considered to be the exit of Q_1. The currents in Q_2 and Q_3 were adjusted to produce an image, both vertical and horizontal, at the target T. Helium filled polyethylene bags were used to cut down air scattering. Their overall effect cannot be stated, but a 25% increase in beam intensity was observed when the bag, external to the shielding wall, was put in place.

The image height measured was 0.8 in. full width at half maximum. The horizontal size was estimated to be $\sim$ 6 in. on the basis of a comparison of counting rate to total π flux out of B. The angular spread vertically in

each beam used - after counter 3 - was 4.5^{o} full width at half maximum.

The lower energy beam was obtained by changing the radial and azimuthal positions of the cyclotron target from the positions for the 87.5 Mev beam. This lowered by 10 Mev the mean energy of the π beam which emerged from the shielding wall. The remaining 8 Mev decrease to 69.5 Mev was obtained by placing lithium and polyethylene absorber in front of counter 1. The 1-2-3 counting rates for the 2 beams were 9000/sec at 87.5 Mev and 3000/sec at 69.5 Mev. The reduction in rate was due entirely to multiple scattering in the additional absorber. These rates include the μ and e contaminations which total 10-15%. It is not necessary to know this contamination precisely since these particles were not counted in the calibration runs because of their range, and they were not present in the scattered beams.

The energy spread in the beam was decreased by placing iron shielding at points 1 and 2 in Fig. 1 since higher energy π's follow a direction tilted with respect to the shielding wall hole. The quoted energy is the energy of a π at the center of the target for $\theta = 0^{o}$. To determine the beam energy precisely, the absorber was adjusted so that the peak of the full energy beam stopped in counter 9. The beam energy was then changed slightly by adjusting the azimuthal position of the cyclotron target. The three central points of the range curve in Fig. 3B were a sensitive test of whether the beam was centered on counter 9.

III. EXPERIMENTAL PROCEDURE

The equivalent copper thickness of the target was measured for each of the three differential cross section curves during the initial calibration of the multicounter. These thicknesses - for normal beam incidence - were the following: 1) For carbon, 0.118 in. and 2) for water plus target holder, 0.125 in.

The thickness of the copper absorber was altered for each value of θ so that the beam of elastically scattered π mesons was centered on counter 9. Consequently, beams of inelastically scattered pions of energies 5, 10, and 15 Mev less than the beam of elastically scattered pions were centered on counters 8, 7, and 6 respectively. During the earlier runs, the elastic beam was centered on counter 8. At the smaller angles where inelastic scattering is small, a check was made that the scattered beam was indeed centered properly since then counters 7 and 9 had approximately the same counting rate. However, less information could be obtained this way and once the system was checked out, the elastic beam was again centered on counter 9.

The energy of the elastically scattered π emanating from the target is a function of θ for two reasons: nuclear recoil and the change in ionization loss of the π due to the increased slant distance traversed in the target by the π with increasing θ. The two effects are of comparable magnitude for the target thicknesses used. Plotted in Fig. 7 is E_π (0°) - E_π (θ) vs θ for the three cases and for hydrogen in the water. The proper copper thickness was calculated accurately, accounting for the

change of relative ionization with energy, and the copper plates were specially ground to give an overall error in absorber thickness of < 0.005 in. of copper or < 0.2 Mev.

The analysis of the data for differential cross sections follows the lines described in BRW. Because of the non-zero energy spread of the beam and the non-zero energy resolution width of the detector, the elastic and inelastic cross sections must be unfolded from the experimental data. One treats the scattered beam as being made up of an elastically scattered beam and three inelastically scattered beams of mean energies 5, 10 and 15 Mev less than the energy of the elastically scattered beam. Each of these beams contributes to the count in each of the counters of the multicounter. The inelastic beams do not actually coincide in mean energy with the energies chosen since they are pions which leave the nuclei in excited final states. The result of the unfolding process is a well determined elastic cross section and inelastic cross sections which give a good indication of scattering from the low lying excited levels of the nucleus. Both carbon and oxygen are well suited to this method as a large separation in energy exists between the ground state and the first excited state, 4.43 Mev for carbon and 6.07 Mev for oxygen. Table II lists the energies of the first several excited levels of carbon and oxygen taken from Ajzenberg and Lauritsen[16].

The method of unfolding is the following: n_9 is the total number of elastically scattered pions; n_8 the total number in the 5 Mev inelastic beam; n_7 the number in the 10 Mev inelastic beam; and n_6 the number in the 15 Mev

inelastic beam. The efficiency matrix element A_{ij} is the probability of a count in counter i if there is one meson in beam j. For example, A_{89} is the relative probability for a count in counter 8 due to an elastic beam of one meson. Table III is a typical efficiency matrix for the 69.5 Mev beam. The experimentally observed count in counter i, corrected for background is

$$n_i' = \sum_{j=6}^{9} A_{ij}\, n_j \quad (i=6\text{-}9).$$

Then $$n_j = \sum_{i=6}^{9} (A^{-1})_{ji}\, n_i' \quad (j=6\text{-}9).$$

n_j will include the effect of all beams which are centered between counters j-1 and j+1, except for n_6 which includes the effect of all beams lower in energy than E_7. n_9 is pure elastic since the scattered beam from the first excited state is almost centered on counter 8 for carbon and is centered between counters 8 and 7 for oxygen.

The statistical error in n_j is due to the errors in n_i' and in A. However, since the errors in n_i' dominate strongly, the errors in A are neglected. The error in n_j is given by

$$\delta n_j = \left\{ \sum_{i=6}^{9} \left[(A^{-1})_{ji} \right]^2 \; (\delta n_i')^2 \right\}^{\frac{1}{2}}$$

$\delta n_i'$ is the statistical error in n_i' including the effect of background.

Consideration has been given to the errors which might be introduced by the unfolding process. This is discussed in Appendix I. From these n_j, the elastic and three inelastic cross sections with errors were calculated on Nevis's IBM 650 computer. At the small angles, it was possible to combine the counts of counters 9 and 8 to measure elastic cross sections without unfolding, since at angles $\theta \leq 55^{\circ}$ the inelastic scattering was negligible. By this means, errors on the small angle data were reduced. This is justified by the extended runs taken at 40° which showed inelastic cross sections that were effectively zero, and by the general trend in inelastic scattering observed at larger θ. Furthermore, the two methods gave the same result at small angles.

There are several small corrections which must be made to these cross sections:

1. π decay in flight. The system was always calibrated with $(D_5)_{min} = 10$ in. Runs were taken varying D_5 between 40 in. and 12 in. One must then correct for all π decays occuring between $(D_5)_{min}$ and D_5. The maximum correction is 7% for $D_5 = 40$ in. One must consider the effect of the decay muons from the pions scattered toward the general region of counter 5. It was determined from an extended range curve that the multicounter did count some muons stopping in it. Hence, it would count some of these decay muons. However, each counter in the multicounter could count no more than 1/16 of all muons passing through counter 5 since the energy spread of these muons was $\sim$ 80 Mev. This is $<$ 1% of the

total π rate.

2. Angular spread. The angular spread of the beam incident on the target was measured to be 4.5^{o} full width at 1/2 maximum for both beams. With the target in, the multiple scattering raised the spread to 5.5^{o} for either target. The linear angular width of counter 5 was folded in quadrature with the beam spread (target in) to give the errors on the angles. This angular width varied from 6.2^{o} to 9.3^{o}. The simplest way to account for the angular spread is to fold it into the theoretical cross section curves which are fit to the data. A gaussian distribution in angle was assumed for the weighting factor. For the curves which were fit by eye to the data, the effect of the angular spread was almost entirely negligible. The χ^2 fit by machine, being more sensitive, required this correction.

3. Change of calibration with θ. The energy of the scattered beam decreases with θ. The copper absorber was decreased correspondingly so that the elastic beam was always centered on counter 9. However, each counter thickness corresponded to a larger energy interval since the specific ionization was increased. Effectively, the efficiency of the whole multicounter increases with θ. The increase is 3.5% at $\theta = 120^{o}$.

4. Hydrogen contamination. The π^- scattering from hydrogen in the water must be accounted for only at the smallest angles in the oxygen scattering. From Fig. 7 it is seen that the energy loss of a π scattered from a

proton increases much faster with increased θ than for a π scattered from oxygen. A correction < 2% is made to the measured elastic count for $20^{o} \leq \theta \leq 30^{o}$. At $\theta = 35^{o}$, this beam is centered between counters 7 and 8 for an elastic beam centered on 9, and for $\theta > 65^{o}$, it is centered in the absorber. Thus, except for n_6, the unfolded count for $\theta \geq 70^{o}$ is the same as it would be were there no hydrogen.

IV. EXPERIMENTAL RESULTS

Differential cross sections are listed in Tables IV, V, and VI for carbon at 69.5 Mev, and 87.5 Mev, and oxygen at 87.5 Mev, respectively. Included in each table are elastic and 5 and 10 Mev inelastic cross sections with their statistical errors. The angular spread for each nominal θ is that calculated from the measured angular spread in the beam, including multiple scattering in the target, and angular acceptance of the beam defining counter 5. Only unfolded cross sections which are considered meaningful are listed so that small angle inelastic scattering is not included. See Appendix I. The small angle elastic cross sections, $\theta \leq 55^{o}$, are, in fact, the non-unfolded ones. These results are shown graphically in Fig. 8, 9, and 10. Fig. 11 is the 80 Mev π^{-} -carbon scattering data of BRW. Theoretical fits to the elastic scattering curves are discussed in Sections V and VI.

A qualitative comparison of the three carbon curves shows a similarity in the behavior of the 5 and 10 Mev inelastic scattering. That is, there is a general increase in the inelastic scattering in the region between 70^{o} and 125^{o}.

The ratio of inelastic to elastic scattering cross section increases from $\lesssim$ 0.1 in the vicinity of 70° to $>$ 1 at the largest angles.

The oxygen inelastic scattering shows a similar behavior at large angles although the statistical accuracy is not as good and the trend is less clear cut. It is evident that at the largest angles the inelastic scattering outweighs the elastic to the point of masking the second minimum in the elastic scattering curve. One, therefore, cannot tell the value of the elastic scattering in this region; but following the arguments of Appendix I again, one can say that the inelastic scattering is several times the elastic. Hence, the elastic cross sections are $\leq$ 1 mb/ster. It is seen that without significant improvement in energy resolution, one will not be able to see clearly the elastic scattering at larger angles.

In BRW, the 5 Mev inelastic scattering is consistently greater than the 10 Mev inelastic although the data for all but the 110° scattering are consistent with equal cross sections. In our 69.5 Mev data, the 10 Mev cross sections are also, for the most part, lower than the 5 Mev inelastic; but the 87.5 Mev carbon data show the two cross sections to be the same within the statistical uncertainties at the larger angles and the 5 Mev scattering to be larger on the average between 70° and 90°. Points which are missing entirely including their error flags are those which unfolded to negative values.

The oxygen data show an indication of a more complex behavior. On the average, 5 Mev scattering predominates over 10 Mev at the largest angles while the reverse is true between 70^{o} and 95^{o} where the uncertainties are very large. Since 10 Mev scattering has contributions from all levels between 6 Mev and 13.7 Mev (See Table II) while 5 Mev scattering has contributions only from those between 6 Mev and 10 Mev, it appears that at the largest angles, the measured average scattering from the lowest levels, 6.06-7.12 Mev, is significantly greater than from the next several levels, 8-14 Mev.

V. OPTICAL MODEL CALCULATIONS

A. Modified Kisslinger Equation Calculations

Calculations of the modified Kisslinger optical model equation discussed in BBR were fit to the data. These were performed on the IBM 650 using the program discussed in that paper.

The wave equation for the meson, including the pion nucleus interaction term, $U\psi$, is

$$\nabla^2\psi + k_o^2\,\psi = \frac{(2E-V_c)V_c}{c^2\,h^2}\,\psi + U\,\psi \qquad \text{(V-1)}$$

V_c is the coulomb potential. The radial equation for angular momentum ℓ is

$$\frac{d^2\phi_\ell}{dr^2} + \left[k_o^2 + \frac{\ell(\ell+1)}{r^2}\right]\phi_\ell$$

$$= \left[1-C_pF\right]\left\{k_o^2\left[(C_p+C_s)\,F + \frac{(2E-V_c)V_c}{(\hbar c k_o)^2}\right]\phi_\ell - C_p\,\frac{dF}{dr}\left(\frac{d\phi_\ell}{dr} - \frac{\phi_\ell}{r}\right)\right\} \qquad \text{(V-2)}$$

The modification from the original Kisslinger theory arises in replacing $\frac{1}{1 + C_pF}$ by $(1-C_pF)$. The following definitions apply: $\hbar k_o$ is the meson momentum in the laboratory system. F(r) is the nuclear density function normalized to F(0) = 1. C_p and C_s are given by

$$C_{p\atop s} = -\frac{4\pi\rho_o}{k_o k_{cm}^2}\left[\frac{Z}{A}\,k_{cm}\,f_P + \frac{N}{A}\,k_{cm}\,f_N\right]_{p\atop s} \qquad \text{(V-3)}$$

where ρ_o is the nuclear density at r = 0 in nucleons/cm^3; $\hbar k_{cm}$ is the π momentum in the center of mass system of the π and a single nucleon when the nucleon is at rest in the laboratory system; A, Z, N are nucleon, proton, and neutron numbers respectively; f_p and f_N are linear combinations of forward coherent scattering amplitudes for π^- - P and π^- - N scattering relative to the pion-nucleon center of mass system, and the subscripts s and p designate that these amplitudes are all s or all p wave.

The parameters C_p and C_s can, in general, be expected to be momentum dependent. This is clearly so because of the momentum dependence of the π-nucleon phase shifts as well

as the explicit dependence in V-3. These two effects tend to cancel for C_p at π energies far enough below the resonance at $\sim$ 193 Mev because of the approximate cubic dependence on momentum of the predominant phase shift, δ_{33}. C_p and C_s were calculated for several values of the incoming pion energy, using the equation of Chew and Low[17] for the momentum dependence of the δ_{33} phase shift and the linear expressions for δ_1 and δ_3. The other 3 phase shifts are set equal to zero. The validity of these forms is discussed Orear[18]. A Fermi type nuclear density distribution was used (Equation V-4 below) with r_o = 1.05f and a = 0.25f. The calculated nuclear parameters are listed in Table VII.

In fitting the calculated cross sections to the data, C_p and C_s (which are complex) and the nuclear size parameters r_o and t, are varied to produce good fits. It will be expected that the best fit C_p and C_s values may agree only roughly with the predicted values because of approximations involved in the formulation of the theory. r_o and t are defined in the usual way: If R is the radius of the nucleus, i.e., the distance from the center to the point where the nuclear density is $\frac{1}{2}$ the central density, then $r_o = R/A^{1/3}$. t is the distance for the nuclear density to fall from 0.9 x central density to 0.1 x central density. The cubic form, V-5, gives a best fit to the 80 Mev carbon data in BRW for r_o = 1.08f and d = 2.0f, while the best fit curve for V-4 was for r_o = 1.08f and a = 0.25f. These two calculated cross section curves are essentially identical. The values of t corresponding to these values for d and a are 1.2f and 1.1f, respectively. This difference is not

considered to be significant since the definition of t is somewhat arbitrary and a slight change in the definition would give a different ratio of the true values of t. Fig. 12 shows a comparison of the two density functions for the same value of r_o, 1.08f, and for d = 2.0f and a = 0.25f.

In the calculations of BBR, the nuclear density function was of the commonly used form

$$F = \frac{1}{1 + e^{\frac{r-R}{a}}} \qquad \text{(V-4)}$$

It was later noted that a more convenient form for computation was the following function for which both F and $\frac{dF}{dr}$ are continuous.

$$F = 1 \qquad r < (R-d/2)$$

$$F = 1/2 - 3/2\left(\frac{r-R}{d}\right) + 2\left(\frac{r-R}{d}\right)^3 \qquad (R-d/2) \leq r \leq (R+d/2) \qquad \text{(V-5)}$$

$$F = 0 \qquad r > (R+d/2)$$

The fall-off parameter for this form is t = 0.60d and the radius for F = 1/2 is R. For form V-4, the radius for F = 1/2 is R and the fall-off is t = 4.4a. The calculated cross sections were adjusted to include the effect of angular spread in the measuring process. The effect of the angular folding was very small but tended slightly to fill in the first minimum in the region of 70^o and to shift it to a larger angle.

For fitting to the data by eye, the goodness of fit is not changed by including the angular folding. In the case of 69.5 Mev scattering from carbon, a more extensive study

was made for the best fit. In this more sensitive test, it becomes necessary to use the angular folding since the position of the minimum is important in determining the nuclear radius R. Fig. 13, 14, and 15 show the elastic cross section data - with the resolution corrected theoretical curves which give the best fits superimposed - for 69.5 Mev carbon, 87.5 Mev carbon, and 87.5 Mev oxygen scattering. Fig. 16 is the 80 Mev data of BRW with the calculation of BBR.

B. Calculation of Best Fit and Standard Deviation of Nuclear Parameters

For the 69.5 Mex carbon data, a χ^2 analysis was performed to determine the parameters giving the best fit to the data. The procedure is as follows:

$$\chi^2(x_i) = \sum_j \delta_j^{-2} \left[G(x_i; \theta_j) - \frac{d\sigma}{d\Omega}(\theta_j) \right]^2 \qquad \text{(V-6)}$$

$\frac{d\sigma}{d\Omega}(\theta_j)$ is the measured cross section at θ; and δ_j is the standard deviation in $\frac{d\sigma}{d\Omega}$. x_i represents a particular set of nuclear parameters: r_o, t, $Re(C_p)$, $Im(C_p)$, $Re(C_s)$, $Im(C_s)$. $G(x_i; \theta_j)$ is the calculated cross section for this set of parameters at θ_j. The parameters which give the best fit, $\bar{x}_i$, are the ones which give rise to the minimum χ^2. Because of the length of time involved in calculating G for a given set of parameters, the following approach was taken. First a best fit to the data was found judging the fit by eye. The parameters for this fit are x_i^o. This was not difficult to obtain since x_i^o are not very different from

the parameters for the 80 Mev carbon fit. Now it is assumed that $\bar{x}_i$ lies close to x_i^o and that $\chi^2(x_i)$ can be expanded in a power series about x_i^o. If the series is terminated at the quadratic terms, we have the following form:

$$\chi^2 = \sum_{i,j=1}^{6} a_{ij} y_i y_j + \sum_{i=1}^{6} b_i y_i + C, \qquad \text{(V-7)}$$

where $y_i = x_i - x_i^o$.

There are a total of 28 independent coefficients in this form which are determined by calculating G for 28 sets of x_i, judiciously chosen so that χ^2 never be so large that higher order terms become important.

Equation V-7 is a paraboloid in seven dimensions and the minimum value of χ^2 is at the point where

$$\frac{d}{dy_i} \chi^2 = \sum_{j=1}^{6} 2a_{ij} y_j + b_i = 0, \text{ for } 1 \leq i \leq 6.$$

The solution of these six simultaneous linear equations gives y_i^o, and $\bar{x}_i = y_i^o + x_i^o$. The value of $\chi^2(\bar{x}_i)$ can be compared to the value obtained by first calculating $G(\bar{x}_i; \theta)$ and then χ^2. That these two values of χ^2 agree very well is a check on the method.

The purpose of this analysis was not primarily to find $\bar{x}_i$. The values one gets are not far from what one gets fitting to the data by eye. Rather, the primary hope was to show that the values of the parameters required to fit the modified Kisslinger equation to the data are well deter-

mined, that the standard deviations for $\bar{x}_i$ are small. For the quadratic form assumed for χ^2, the standard deviation for the parameter x_k is

$$\sigma_k = \left[(a^{-1})_{kk}\right]^{\frac{1}{2}}$$

where a^{-1} is the inverse matrix to a_{ij}.

[The above formula has an interesting geometrical interpretation. It can be shown that σ_k is the maximum value of $| x_k - \bar{x}_k |$ on the ellipsoid $\chi^2 = \chi^2_{min} + 1$. It must be remembered that this is true only for the quadratic form for χ^2.]

The minimum χ^2 expected on the basis of statistical theory for 22 points and 6 parameters is 16 ± 6. The minimum χ^2 obtained from the analysis was 16.9 and the χ^2 obtained from G $(\bar{x}_i; \theta)$ was also 16.9. This shows excellent consistency.

The values of $\bar{x}_i$ together with σ_i are listed in Table VIII along with the best fit parameters for the 87.5 Mev carbon and the 87.5 Mev oxygen scattering, and the 80 Mev carbon data of BRW.

C. Kroll Equation Calculations

The Kroll equation is a refinement of the unmodified Kisslinger equation which leads to the radial equation

$$\frac{d^2\phi_\ell}{dr^2} + \left[k_o^2 + \frac{\ell\,(\ell+1)}{r^2}\right]\phi_\ell \qquad \text{(V-8)}$$

$$= (1 + 2/3\ C_pF)^{-1}\left[k_o^2\left\{\left[C_p+C_s\ (1-1/3\ C_pF)\right]\ F + \frac{(2E-V_c)\ V_c\ (1-1/3\ C_pF)}{(\hbar c k_o)^2}\right\}\phi_\ell - \frac{C_p\ \frac{dF}{dr}}{1-1/3\ d_pF}\left(\frac{d\phi_\ell}{dr} - \frac{\phi_\ell}{r}\right)\right]$$

The quantities are defined as above. As has been reported by Rainwater[19], this form has been used in an attempt to fit the 80 Mev carbon data. Close to good agreement was obtained but not as good as with the modified Kisslinger equation. Several attempts have been made to fit the present data, although a systematic study has not been made. Good fits have not been obtained.

VI. DISCUSSION

A. Comparison of Elastic Cross Sections

There are several regularities to be noticed in the data of this experiment and the one of BRW. They are by and large the ones to be expected in diffraction scattering. Due to the improved technique, the diffraction patterns and the regularities in them are more clearly apparent than in any other experiment to date.

Born approximation type calculations have had moderate success predicting π-nucleus scattering [2-5]. In particular, one can obtain back angle cross sections which hold up. The qualitative features of the approximation are in agreement with the general trends observed in these experiments. The

scattering amplitude in this approximation is of the form

$$\phi(\underset{\sim}{q}) = t_{\underset{\sim}{q}} \cdot A \cdot f(\underset{\sim}{q}). \qquad \text{(VI-1)}$$

$\underset{\sim}{q}$ is the momentum transfer ($q = 2k \sin \theta/2$), $\hbar k$ is pion momentum, $t_{\underset{\sim}{q}}$ is the scattering amplitude from the "average" nucleon, and $f(\underset{\sim}{q})$ is the nuclear form factor. In the quantitative application of this form, the scattering amplitude must be evaluated at the kinetic energy appropriate to the interior of the nucleus and account taken of the nucleon Fermi momentum, and of the fact that the scattering is elastic with respect to the nucleus as a whole. (See reference 3.) In this qualitative discussion these refinements are neglected.

For scattering at energies well below the (3/2, 3/2) resonance

$$t_{\underset{\sim}{q}} = C_s k^2 + C_p k^2 \cos \theta \qquad \text{(VI-2)}$$

where $C_s k^2$ and C_p are nearly constant with pion momentum, k. $C_s k^2$ gives the s-wave, and $C_p k^2 \cos \theta$, the p-wave contribution to the scattering. (Spin flip terms are omitted from $t_{\underset{\sim}{q}}$ as not contributing to the coherent scattering.) For most of the small angle region except close to the first minimum, $\phi(\underset{\sim}{q})$ increases as k does, since at these energies the p-wave term dominates and $t_{\underset{\sim}{q}}$ increases with k faster than $f(\underset{\sim}{q})$ decreases. At small angles, the dependence of $f(\underset{\sim}{q})$ on atomic number A is slow compared to the explicit term A, so ϕ increases with A. The diffraction pattern is determined for the most part by $f(\underset{\sim}{q})$. Since f depends approximately on $qR \propto qA^{1/3}$, an increase in either k or A shifts the pattern, in particular the minima, to smaller angles.

Due to the signs of $Re(C_p)$ and $Re(C_s)$, $|t_{\tilde{q}}|$ has a minimum in the region of 70^o - 80^o and then rises to values at large angles which exceed the forward angle values. This tendency to increase holds up the large angle scattering against the general tendency of $f(\tilde{q})$ to decrease in this region.

Fig. 17 shows the best fits to the three sets of carbon data superimposed for ease of comparison. In the small angle region, there is a small but significant increase in cross section between the 69.5 Mev data and the 87.5 Mev data. The 80 Mev data cannot be distinguished from the 87.5 Mev data in this region but the difference will be small in any case. There is no clear cut shift in position of the first dip at $\sim 70^o$ with energy, but the second dip shows the expected regularity. The data do not fully show the second dip but can be said to support and be entirely consistent with the shift in this dip.

In the sequence Li, C, O, Al, Cu, the cross sections at small angles show a consistent increase with A at small angles - for $\theta \geq 35^o$ Coulomb interference becomes negligible. Also, the first and second diffraction dips occur at successively smaller angles. For Li, the second dip is not seen but it is obvious that it must appear at a larger angle than for C if it occurs at all at this energy. As with C, the second dip in O is not fully seen, but the data are consistent with an appearance at the proper place. It must be noted, also, that the Al and Cu data included unknown amounts of inelastic scattering. This contribution is probably small for angles below the first dip.

B. Optical Model Theory

Earlier attempts [4-6,11,20] have been made to fit an optical model differential equation to the data of π-nucleus scattering using a complex square well potential of the form V + i W. In the optical theory of Watson and Francis[21,22] for uniform nuclear matter, the potential is proportional to the product of the nuclear density and the coherent forward scattering amplitude for π scattering from the "average" nucleon. From the optical theorem, then, W is proportional to the total cross section for π-nucleon scattering. Modifications should then be made to W to include the increase due to pion absorption by deuteron pairs and the decrease due to the Pauli principle, i.e., elimination of already occupied phase space for the recoil nucleon. For a finite nucleus, and especially for light nuclei whose diameters are of the order of a pion wavelength, the scattered wave becomes spread out to large angles and is therefore sensitive to the π-nucleon scattering amplitude in other than the forward direction. An optical potential of the form

$$(V + i\,W)\ \rho\ (\underset{\sim}{r}) \qquad \text{(VI-3)}$$

where ρ is nucleon density, implies isotropic scattering from an individual scatterer, for a finite nucleus. This is clearly not the case for π-nucleon scattering since the p-wave term dominates at these energies. The early attempts were successful in fitting the scattering data in the small angle region only, and the fits were obtained using values of $r_o \approx 1.4$ fermis. BBR attempted to fit the BRW data using VI-3 but the minima predicted were consis-

tently too deep and the best fits to the small angle data again gave $r_o \approx 1.4$ fermis. Roughly speaking and with reference to the Born approximation again, the larger radius arises because the fall-off in the small angle region is provided wholely by the nuclear form factor whereas actually some is provided by the decrease in $|t_{\underset{\sim}{q}}|$ which passes through a minimum near 70^o. To obtain this more rapid rate of decrease in $f(\underset{\sim}{q})$, one must choose a larger nuclear radius.

Neglecting the Coulomb interaction, the Kisslinger theory uses the wave equation

$$\nabla^2\psi + k_o^2\psi = U\psi = C_s k_o^2 F\psi - C_p \nabla \cdot F \nabla \psi. \qquad \text{(VI-4)}$$

In principle, as discussed by BBR, $C_s k_o^2$ is roughly independent of $-\nabla^2\psi/\psi = k^2_{eff}$, the square of the effective momentum. For low k^2_{eff}, one also has C_p effectively independent of k^2_{eff}, and, in the unmodified Kisslinger theory, one makes it strictly independent of k^2_{eff}. In fact, the p-wave interaction passes through resonance at $\sim$ 193 Mev where $\mathrm{Re}(C_p) \to 0$. Thus, as k^2_{eff} approaches this region, $\mathrm{Re}(C_p) \to 0$. The term $C_p \nabla \cdot F \nabla \psi$ involves a part $C_p F \nabla^2\psi$ which is combined with the kinetic energy term $\nabla^2\psi$. Rearranging the equation, one gets

$$\nabla^2\psi + k_o^2\psi = U'\psi = \frac{[(C_s+C_p)\, k_o^2 F\psi - C_p \nabla F \cdot \nabla \psi]}{1 + C_p F} \qquad \text{(VI-5)}$$

This gives a "feedback" denominator term $(1 + C_p F)$. If the value of C_p appropriate to $\nabla^2\psi/\psi = -k_o^2$ is used, the real part of $C_p F$ tends to be negative inside the nucleus so

$\mathrm{Re}(1 + C_p F)$ is negative and the effective sign of the apparent interaction actually reverses as F goes to 0. However, as one gradually "turns on" the $(1 + C_p F)$ denominator term (gradually changes it from unity), the value of $|\nabla^2 \psi/\psi|$ increases and this implies a decreased $|\mathrm{Re}(C_p)|$. The feedback cannot give a sign reversal, since as $\nabla^2 \psi/\psi$ approaches its value corresponding to the (3/2, 3/2) resonance, $|\mathrm{Re}(C_p)| \to 0$, if the detailed behavior of C_p on $\nabla^2 \psi/\psi$ is used properly. This suggest the following:

1) The apparent "blow up" effect of $(1 + C_p F)$ reversing the sign of U^{ℓ} is not real. The standard modification of the Kisslinger theory which we have adopted tries to take this qualitative feature into account by the arbitrary feature of replacing $(1 + C_p F)^{-1}$ by $(1 - C_p F)$. The simplification is retained of using a value of C_p, which is independent of $\nabla^2 \psi/\psi$ for a given nucleus and k_o.

2) Since $|\nabla^2 \psi/\psi| > k_o^2$ within the nucleus, it is proper to use a value of (fixed) C_p and C_s appropriate to some higher effective kinetic energy within the nucleus, rather than the values for k_o^2. This implies a smaller $|\mathrm{Re}(C_p)|$ and a larger $|\mathrm{Im}(C_p)|$. Our best fitting C_p differs from that implied from pion-nucleon scattering at k_o^2 exactly in this manner. Since it is difficult to evaluate this effect precisely, we are forced to regard C_p and C_s as adjustable parameters determined only roughly by pion nucleon scattering.

3) For low k_o^2, the ratio $-\nabla^2 \psi/k_o^2 \psi$ can be larger without having $\nabla^2 \psi/\psi$ reach the (3/2, 3/2) resonance region. Thus, larger $|\mathrm{Re}(C_p)|$ is permitted than for larger k_o^2 where a

smaller ratio of $-\nabla^2\psi/k_o^2\psi$ is permitted. We, in fact, find a best match C_p for 69.5 Mev with $|Re(C_p)|$ significantly larger than for 87.5 Mev.

A more precise treatment of VI-5 or of the corresponding Kroll equation would involve determining, at each radius point, a self-consistent set of values for C_p and C_s which, when inserted in the right side, lead to a predicted $\nabla^2\psi/\psi$ consistent with this choice of C_p and C_s. The dependence of C_p and C_s for pion-(average) nucleon scattering is shown in Table VII.

The optical wave equation of Kroll is a refinement of the Kisslinger theory which in its mathematical form lies intermediate between the unmodified form and the modified one of BBR. In relating the optical properties of a dielectric medium to those of the individual constituents, a distinction is made between the average electric field at a scatterer and the effective field. (Lorentz-Lorenz theory.) A similar distinction may be made in π-nucleus scattering. Kroll's potential attempts to take account of this difference. Whereas the modified Kisslinger theory is obtained by replacing $(1 + C_pF)^{-1}$ by $(1 - C_pF)$, Kroll's equation is nearly what would result by using $(1 + 2/3\ C_pF)^{-1}\ (1 - 1/3\ C_pF)$ which also reduces, but does not necessarily overcome, the tendency of the interaction to diverge.

Since Kroll's modification of the Kisslinger equation does not take account of the divergence features discussed above, and since his equation is intermediate in form between the modified and unmodified Kisslinger equations,

the modified equation may be regarded as an approximation for the Kroll equation as well.

C. Nuclear Parameters

The simpler discussion in terms of the Born approximation, while descriptive of the gross features of the elastic scattering data, does not account for them quantitatively. The exact solution of the optical model equation, as has been seen, is capable of giving excellent agreement with the data when the parameters C_p and C_s are treated phenomenologically.

A comparison of Tables VII and VIII shows that $\mathrm{Re}(C_p)$ for best fit indeed corresponds to that predicted for higher kinetic energy ($\sim$140 Mev). $\mathrm{Im}(C_p)$, $\mathrm{Re}(C_s)$, and $\mathrm{Im}(C_s)$ have the expected signs but are different in magnitude from what would be expected from an inspection of Table VII setting E $\sim$140 Mev. The values of $\mathrm{Im}(C_p)$ and $\mathrm{Im}(C_s)$ are apt to be strongly influenced by effects (virtual deuteron type absorption and Pauli principle effects) not present in ordinary pion nucleon scattering. Breuckner (private discussions) has suggested that it might even be appropriate to lump the absorption contribution of C_p in the C_s type terms. Thus it is difficult to decide just what values of $\mathrm{Im}(C_p)$ and $\mathrm{Im}(C_s)$ would be favored a priori. The $\mathrm{Re}(C_s)$ term is larger than predicted but is still much smaller than $|\mathrm{Re}(C_p)|$. It is interesting to point out that the usual (older) optical model results by setting $C_p = 0$ and only using a term of the form C_s (which also includes the effect of p-wave scattering). Thus the fact that the favored value of $|\mathrm{Re}(C_p)|$ is appreciably

greater than $|Re(C_s)|$ may be interpreted as indicating the importance of including the $\nabla F \cdot \nabla\psi$ type terms which are characteristic of the p-wave elementary scattering process. The value of $Re(C_s)$ is found to increase with decreasing k_o^2 in such a way as to maintain the expected energy independence of $C_s k_o^2$ on k_o^2. A comment should be made on the expected change in $Re(C_s)$ for a given k_o^2 due to the higher effective k^2 inside the nucleus. Although C_s in Table VII decreases with k^2, the tabulated values should be multiplied by (k^2/k_o^2) to evaluate $C_s k_o^2$ inside the nucleus. Thus the expected C_s inside the nucleus is that for the outside k_o^2, if no further complications are present.

The modified Kisslinger equation is also seen to fit all values of data for different nuclei (Li, C, O) with essentially the same C_p and C_s for a given energy independent of A.

The radius and fall-off parameters, r_o and t, given by this model, are consistently the same for all the data which have been fit. Furthermore, the least squares analysis of the 69.5 Mev data shows that the best fitting values for our particular wave equation have been determined with good precision. The errors arise only from the statistical errors in the experiment. The radius determined here is consistent with the radius determined by electron scattering[14], the best value of which is $r_o = 1.07$f. The fall-off parameter, t, obtained from electron and proton scattering is consistently in the region 2.0 - 2.5f while the one obtained in this experiment is 1.16f, roughly 1/2 the above value. Ravenhall[14]

has calculated a 13% difference between t for proton center of mass and t for charge. If the pion interacts principally with the bare nucleon the disagreement is reduced, but the inability of the model to predict a larger t indicates a shortcoming in the form of the wave equation. The modifications which should, in principle, be made to the wave equation have been discussed in VI-B.

VII. ACKNOWLEDGEMENT

The author wishes to thank Prof. J. Rainwater for his esteemed guidance throughout the experiment and Dr. W. Baker for his valued collaboration.

APPENDIX I

The Unfolding Process

The unfolding process replaces beams scattered from excited levels by beams whose mean energies are 5, 10, and 15 Mev below the mean energy of the elastic beam. For example, the beam scattered from the 7.65 Mev level in carbon is replaced by beams whose energies are 5 and 10 Mev below the elastic beam energy. Suppose that all scattering is from one level whose energy is $(d_1 + \alpha)$ Mev above the ground state. See. Fig. A-1. d_1, d_2, and d_3 are the separations between the mean energies of the beams which would be centered on the 4 counters. They are not necessarily equal but are almost so. They are also almost equal to 5 Mev. It is also assumed that the resolution function for counter i is $\exp\{-p_i |E-E_i|\}$ where the counters may have different decay constants, p_i. E is the mean energy of a beam, and E_i is the mean energy of the beam centered on counter i. See Fig. 3-B. The counting rate in each counter will be

$$n_6' = FN_6 e^{-p_6(d_1+d_2-\alpha)} = N_6 \left[F_7' e^{-p_6 d_1} + F_8' e^{-p_6(d_1+d_2)}\right] \quad \text{(A-1)}$$

$$n_7' = FN_7 e^{-p_7(d_2-\alpha)} = N_7 \left[F_7' + F_8' e^{-p_7 d_2}\right] \quad \text{(A-2)}$$

$$n_8' = FN_8 e^{-p_8\alpha} = N_8 \left[F_7' e^{-p_8 d_2} + F_8'\right] \quad \text{(A-3)}$$

$$n_9' = FN_9 e^{-p_9(d_3+\alpha)} = N_9 \left[F_7' e^{-p_9(d_2+d_3)} + F_8' e^{-p_9 d_3}\right] \quad \text{(A-4)}$$

F is the total number of pions in the beam; N_i is the efficiency of counter i for a beam centered on it: F_7' and F_8' are the equivalent beams, centered on counters 7 and 8, which replace F. In order to show that the unfolding process is correct, one need only show that the above four equations in the two unknowns, F_7' and f_8', are compatible.

In the ideal case, $d_1 = d_2 = d_3$, all p_i are equal and N_i are equal. In this case, (A-1) and (A-2) are related by a multiplicative constant as are (A-3) and (A-4). Thus there are effectively two equations in two unknowns, and

$$F_7' = \frac{\sinh p\alpha}{\sinh pd}, \qquad \text{(A-5)}$$

$$F_8' = \frac{\sinh p(d-\alpha)}{\sinh pd} \qquad \text{(A-6)}$$

Since (A-1) through (A-4) are linear equations, in the ideal case it is always possible to apply this procedure to several randomly placed beams simultaneously.

In the following, various deviations from the ideal case are considered:

1. The resolution function is not exactly of the exponential form. The central portion approximates it closely, but the tails are significantly larger. This is the region where efficiency is less than 10% peak efficiency. In order that a tail of a strong beam produce a large error (greater than 20%) in a nearby weak beam, the former must be at least 3 times as strong as the weak one. For larger factors, deviations in the central portions will be significant. At the same time, the statistical error

for the smaller cross section is increasing so it is clear to see the regions where this effect is important. At the largest angles in the oxygen scattering, the large inelastic cross sections mask the elastic. At small angles in all the curves, the elastic masks the inelastic. The method is most reliable for obtaining both elastic and inelastic for carbon between 70^{o} and 125^{o} and for oxygen between 70^{o} and 110^{o}. At the smaller angles, the elastic cross section is well determined.

2. The peak efficiencies N_i were not equal. This contributes no error as can be seen from the following. The efficiency matrix is A. If this were altered to produce equal peak efficiencies, the efficiency matrix would then be $A' = CA$, where C is a matrix whose elements are $C_{ij} = c_j$. But the experimentally observed counting rate would be

$$n_i'' = \sum_{j=6}^{9} C_{ij}\, n_j'. \quad \text{Thus}$$

$$\underset{\sim}{n}'' = C\underset{\sim}{n}' = A'\underset{\sim}{n} = CA\underset{\sim}{n} \qquad \text{and}$$

$$\underset{\sim}{n} = (A')^{-1}\underset{\sim}{n}'' = A^{-1}\underset{\sim}{n}'.$$

3. If the only deviation from the ideal case is that d_1, d_2 and d_3 are unequal, there is no error introduced. For if the p_i are all equal, (A-1) and (A-2) are related by a constant multiplier as are (A-3) and (A-4) as in the ideal case. This would also be true if $p_9 = p_8$, $p_7 = p_6$. This latter condition is very close to the case for the multicounter as used.

4. Suppose $d_1 = d_2 = d_3$ but that $p_9 = p_8 + \epsilon_{98}$ and $p_6 = p_7 + \epsilon_{67}$. Then (A-1) through (A-4) are not consistent but one can solve for F_7' and F_8' using any of the following pairs of equations; (A-1) and (A-3), (A-1) and (A-4), (A-2) and (A-3), and (A-2) and (A-4). Experimentally $|\epsilon_{98}| < 0.1\ p_9$ and $|\epsilon_{67}| < 0.1\ p_6$. Then the various solutions of F_7' agree within 10%, and for F_8' within 10% also. This is less than the statistical error on these numbers. (The elastic count does not involve such a problem since it is always centered on a counter.)

FOOTNOTES

[1] W. F. Baker, J. Rainwater, R. E. Williams, Phys. Rev. 112, 1763 (1958).

[2] A. Pevsner, J. Rainwater, R. E. Williams and S. J. Lindenbaum, Phys. Rev. 100, 1419 (1955).

[3] R. E. Williams, J. Rainwater and A. Pevsner, Phys. Rev. 101, 412 (1956).

[4] R. E. Williams, W. F. Baker, J. Rainwater, Phys. Rev. 104, 1695 (1956).

[5] H. Byfield, J. O. Kessler, L. M. Lederman, Phys. Rev. 86, 17 (1952).

[6] J. O. Kessler and L. M. Lederman, Phys. Rev. 94, 689 (1954).

[7] G. Saphir, Phys. Rev. 104, 535 (1956).

[8] J. F. Streib, Phys. Rev. 100, 1797 (1955).

[9] K. Strauch and F. Titus, Phys. Rev. 104, 191 (1956).

[10] P. P. Kane, Phys. Rev. 112, 1337 (1958).

[11] T. A. Fujii, Phys. Rev. 113, 695 (1959).

[12] W. F. Baker, H. Byfield, J. Rainwater, Phys. Rev. 112, 1773 (1958).

[13] L. S. Kisslinger, Phys. Rev. 98, 761 (1955).

[14] D. G. Ravenhall, Rev. Mod. Phys. 30, 430 (1958).

[15] N. M. Kroll (private communication).

[16] F. Ajzenberg and T. Lauritsen, Rev. Mod. Phys. 27, 77 (1955).

[17] G. F. Chew and F. E. Low, Proceedings of the Fifth Rochester Conference (Interscience Publishers, Inc. New York, 1955).

[18] J. Orear, Phys. Rev. 100, 288 (1955).

[19] J. Rainwater, Proceedings of the International Conference on the Nuclear Optical Model (Florida State University, 1959).

[20] A. Pevsner, J. Rainwater, Phys. Rev. 100, 1431 (1955).

[21] K. M. Watson, Phys. Rev. 89, 575 (1953).

[22] N. C. Francis, K. M. Watson, Phys. Rev. 92, 291 (1953).

Table I.

Counter dimensions

Counter	Height	Width	Thickness
1	2 "	4 "	1/4 "
2	1-1/4	4	1/4
3	3/4	3	1/4
4	2-1/2	7	1/4
5	2	6	1/4
6	4-1/2	8	3/8
7	5	8-1/2	3/8
8	5-1/2	9	3/8
9	6	9-1/2	3/8
10	6-1/2	10	3/8

Table II.

Levels of excitation energy less than 15 Mev in Carbon and Oxygen

(From Ajzenberg and Lauritzen)

Carbon	Oxygen
4.43 Mev	6.06 Mev
7.65	6.14
9.61	6.91
10.8	7.12
11.1	8.6
11.74	9.58
12.76	9.84
13.3	10.36
14.16	11.10
15.09	11.25
	11.51
	11.62
	12.43
	12.51
	12.95
	13.09
	13.24
	13.65

Table III.

Typical efficiency matrix for 69.5 Mev beam

Counter in which beam is centered \ Counter	% of incident beam counted			
	6	7	8	9
6	27.03	10.01	2.41	1.44
7	11.27	31.72	9.31	2.41
8	2.75	12.62	27.74	9.54
9	1.81	3.40	9.24	30.15

Table IV.

69.5 Mev Carbon Cross Sections

θ	Elastic	5 Mev Inelastic	10 Mev Inelastic
20 ± 3.1°	147. ± 16.		
25 ± 3.1°	93. ± 9.		
30 ± 3.1°	79.1 ± 6.6		
35 ± 3.1°	50.5 ± 4.7		
40 ± 3.1°	41.5 ± 3.5		
45 ± 4.0°	26.9 ± 2.0		
50 ± 4.0°	14.9 ± 1.2		
55 ± 4.0°	8.9 ± 1.0		
60 ± 4.0°	5.08 ± 0.56	0.58 ± 0.56	0.31 ± 0.48
65 ± 4.0°	4.15 ± 0.33	*	0.12 ± 0.29
70 ± 4.7°	3.21 ± 0.25	*	0.44 ± 0.25
75 ± 4.7°	4.06 ± 0.31	*	0.41 ± 0.25
80 ± 4.7°	4.48 ± 0.71	0.66 ± 0.68	*
85 ± 4.7°	4.89 ± 0.50	0.76 ± 0.45	*
90 ± 4.7°	5.07 ± 0.83	*	*
95 ± 4.7°	5.23 ± 0.32	1.04 ± 0.32	1.22 ± 0.29
100 ± 4.7°	5.34 ± 0.62	1.81 ± 0.65	0.53 ± 0.54
105 ± 4.7°	4.38 ± 0.53	1.58 ± 0.58	1.39 ± 0.52
110 ± 4.7°	4.91 ± 0.58	2.35 ± 0.65	1.44 ± 0.58
115 ± 4.7°	3.37 ± 0.48	2.68 ± 0.60	1.61 ± 0.56
120 ± 4.7°	3.16 ± 0.47	3.39 ± 0.61	1.54 ± 0.57
125 ± 4.7°	2.16 ± 0.44	3.70 ± 0.64	3.18 ± 0.63

*Unfolds to negative cross sections

Table V.

87.5 Mev Carbon Cross Sections

θ	Elastic	5 Mev Inelastic	10 Mev Inelastic
25 ± 2.8°	109.2 ± 10.6		
30 ± 2.8°	86.0 ± 6.1		
35 ± 2.8°	68.4 ± 4.9		
40 ± 2.8°	39.8 ± 1.8		
45 ± 3.8°	29.0 ± 2.6		
50 ± 3.8°	15.0 ± 1.0		
55 ± 3.8°	7.79 ± 0.51		
60 ± 3.8°	5.80 ± 0.49	0.53 ± 0.48	0.24 ± 0.38
65 ± 3.8°	4.18 ± 0.34	0.45 ± 0.33	0.08 ± 0.27
70 ± 3.8°	3.46 ± 0.29	0.07 ± 0.30	0.39 ± 0.27
75 ± 4.5°	3.63 ± 0.26	0.05 ± 0.25	0.32 ± 0.21
80 ± 4.5°	4.07 ± 0.44	0.19 ± 0.37	0.24 ± 0.31
85 ± 4.5°	3.57 ± 0.51	0.73 ± 0.47	0.36 ± 0.38
90 ± 4.5°	3.30 ± 0.30	0.96 ± 0.32	0.65 ± 0.28
95 ± 4.5°	2.78 ± 0.40	1.01 ± 0.42	1.07 ± 0.39
100 ± 4.5°	2.60 ± 0.31	1.53 ± 0.37	1.72 ± 0.36
105 ± 4.5°	1.72 ± 0.26	1.67 ± 0.33	1.77 ± 0.33
110 ± 4.5°	1.16 ± 0.23	1.97 ± 0.33	2.08 ± 0.34
115 ± 4.5°	0.80 ± 0.29	2.38 ± 0.49	2.07 ± 0.50
120 ± 4.5°	0.90 ± 0.28	2.03 ± 0.47	2.66 ± 0.51
125 ± 4.5°	0.61 ± 0.26	2.41 ± 0.45	2.25 ± 0.47

Table VI.

87.5 Mev Oxygen Cross Sections

θ	Elastic	5 Mev Inelastic	10 Mev Inelastic
20 ± 2.8^{o}	$230. \pm 11.$		
25 ± 2.8^{o}	$162. \pm 9.$		
30 ± 2.8^{o}	$110. \pm 8.$		
35 ± 2.8^{o}	75.3 ± 4.3		
40 ± 2.8^{o}	54.1 ± 2.5		
45 ± 3.8^{o}	27.2 ± 2.2		
50 ± 3.8^{o}	17.1 ± 0.9		
55 ± 3.8^{o}	8.4 ± 0.7		
60 ± 3.8^{o}	5.8 ± 1.1	0.97 ± 0.99	1.10 ± 0.86
65 ± 3.8^{o}	4.23 ± 0.71	0.56 ± 0.62	1.00 ± 0.51
70 ± 3.8^{o}	4.42 ± 0.60	0.37 ± 0.57	0.35 ± 0.90
75 ± 4.5^{o}	4.15 ± 0.62	*	1.10 ± 0.33
80 ± 4.5^{o}	3.21 ± 0.88	0.05 ± 0.81	1.48 ± 0.58
85 ± 4.5^{o}	3.07 ± 0.55	0.78 ± 0.45	2.05 ± 0.41
90 ± 4.5^{o}	2.29 ± 0.42	1.58 ± 0.47	*
95 ± 4.5^{o}	2.44 ± 0.46	0.20 ± 0.44	2.61 ± 0.44
100 ± 4.5^{o}	0.59 ± 0.33	2.10 ± 0.48	1.44 ± 0.72
105 ± 4.5^{o}	*	2.14 ± 0.35	2.41 ± 0.30
110 ± 4.5^{o}	0.29 ± 0.32	2.79 ± 0.47	2.56 ± 0.76
115 ± 4.5^{o}	*	2.69 ± 0.38	2.62 ± 0.34
120 ± 4.5^{o}	0.25 ± 0.32	2.54 ± 0.46	1.44 ± 0.87
130 ± 4.5^{o}	0.09 ± 0.45	3.93 ± 0.82	2.55 ± 0.86

*Unfolds to negative cross sections

Table VII.

Strength Parameters vs. Piøn Energy

Pion Kinetic Energy (Lab)	C_p	C_s	Element
70	-1.83 - 0.38i	0.093 - 0.097i	Carbon
80	-1.88 - 0.52i	0.081 - 0.089i	
87.5	-1.88 - 0.62i	0.073 - 0.085i	
100	-1.86 - 0.84i	0.063 - 0.078i	
130	-1.55 - 1.53i	0.046 - 0.065i	
160	-0.47 - 2.01i	0.036 - 0.057i	
70	-1.86 - 0.39i	0.095 - 0.098i	Oxygen
80	-1.91 - 0.53i	0.082 - 0.091i	
87.5	-1.91 - 0.63i	0.074 - 0.086i	
100	-1.89 - 0.85i	0.064 - 0.079i	
130	-1.58 - 1.55i	0.047 - 0.066i	
160	-0.48 - 2.05i	0.037 - 0.058i	

Table VIII.

Nuclear Parameters for Best Fit to Data

69.5 Mev Carbon

$r_o = 1.053 \pm 0.020$ fermis

$t = 1.16 \pm 0.07$ fermis

$C_p = (-1.395 \pm 0.036) + i(-0.063 \pm 0.010)$

$C_s = (0.451 \pm 0.003) + i(-0.145 \pm 0.018)$

80 Mev Carbon (from BRW)

$r_o = 1.08$ f

$t = 1.2$ f

$C_p = 1.1 - 0.1i$

$C_s = + 0.35 - 0.15i$

87.5 Mev Carbon

$r_o = 1.08$ f

$t = 1.2$ f

$C_p = -1.1 - 0.15i$

$C_s = + 0.35 - 0.15i$

87.5 Mev Oxygen

$r_o = 1.08$ f

$t = 1.2$ f

$C_p = -1.05 - 0.10i$

$C_s = + 0.40 - 0.15i$

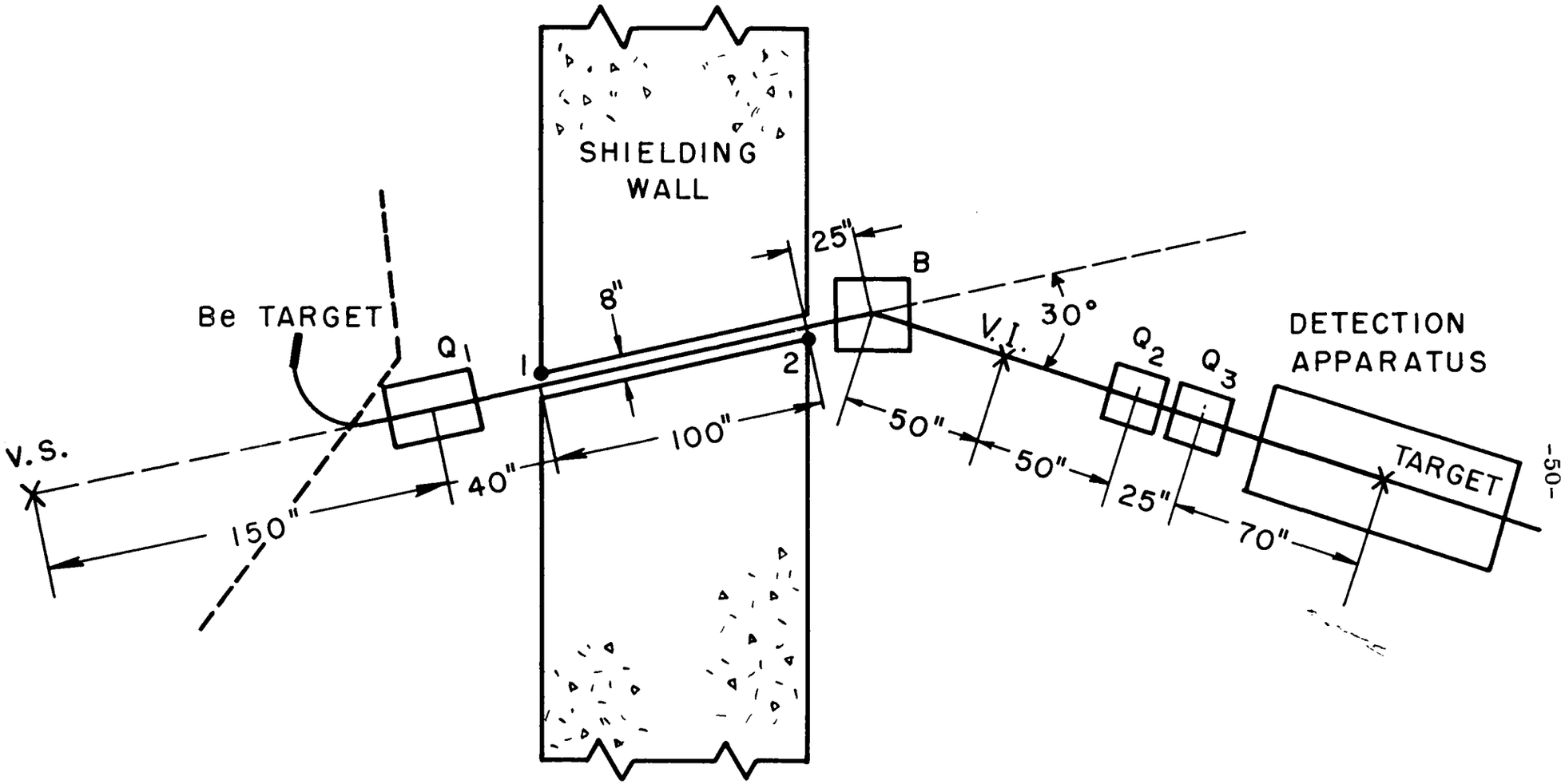

GENERAL EXPERIMENTAL LAYOUT

FIG. 1

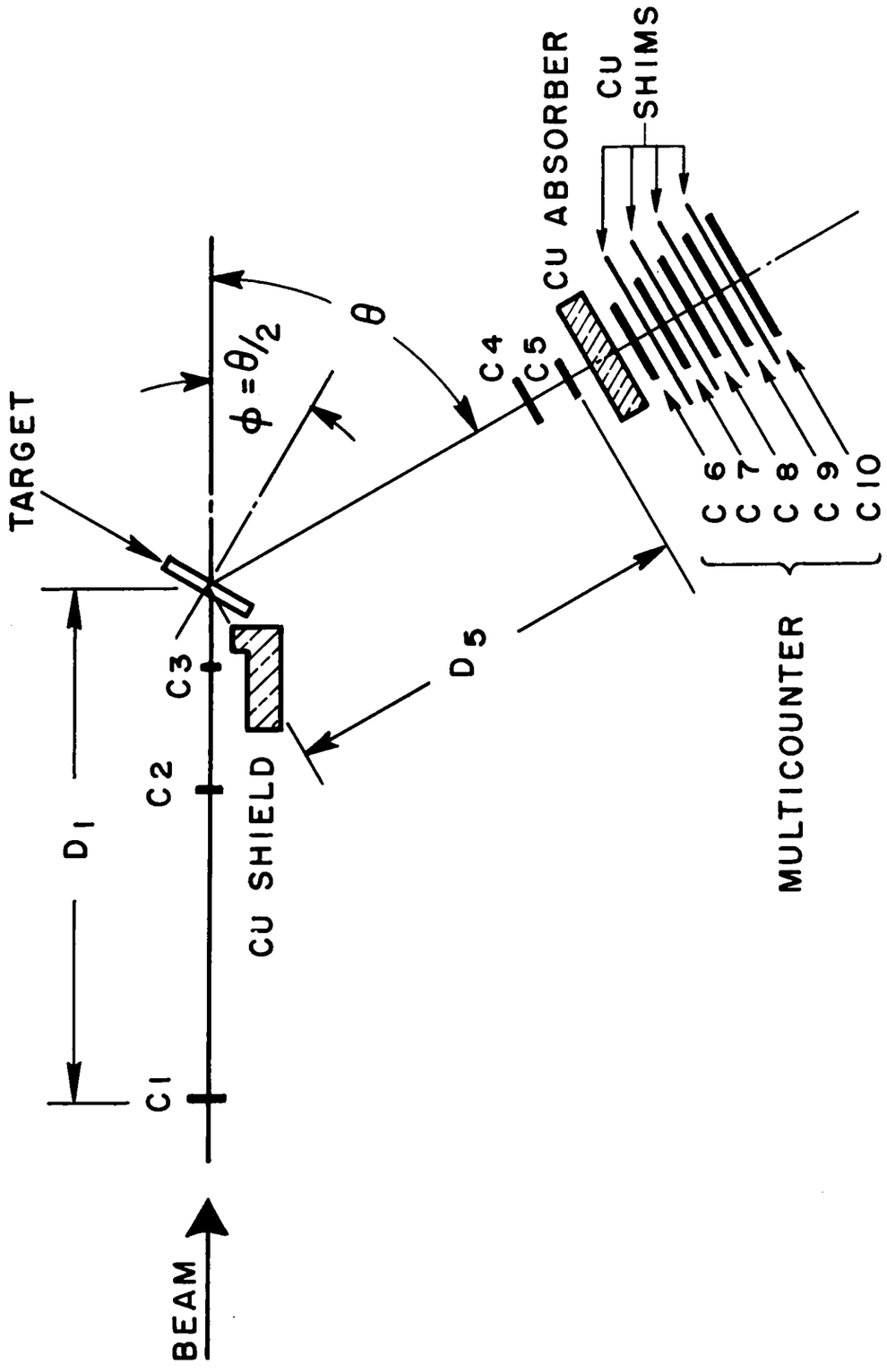
TARGET
BEAM
C1
C2
C3
C4
C5
C6
C7
C8
C9
C10
D1
D5
θ
φ=θ/2
CU SHIELD
CU ABSORBER
CU SHIMS
MULTICOUNTER
COUNTER ARRANGEMENT

FIG 2

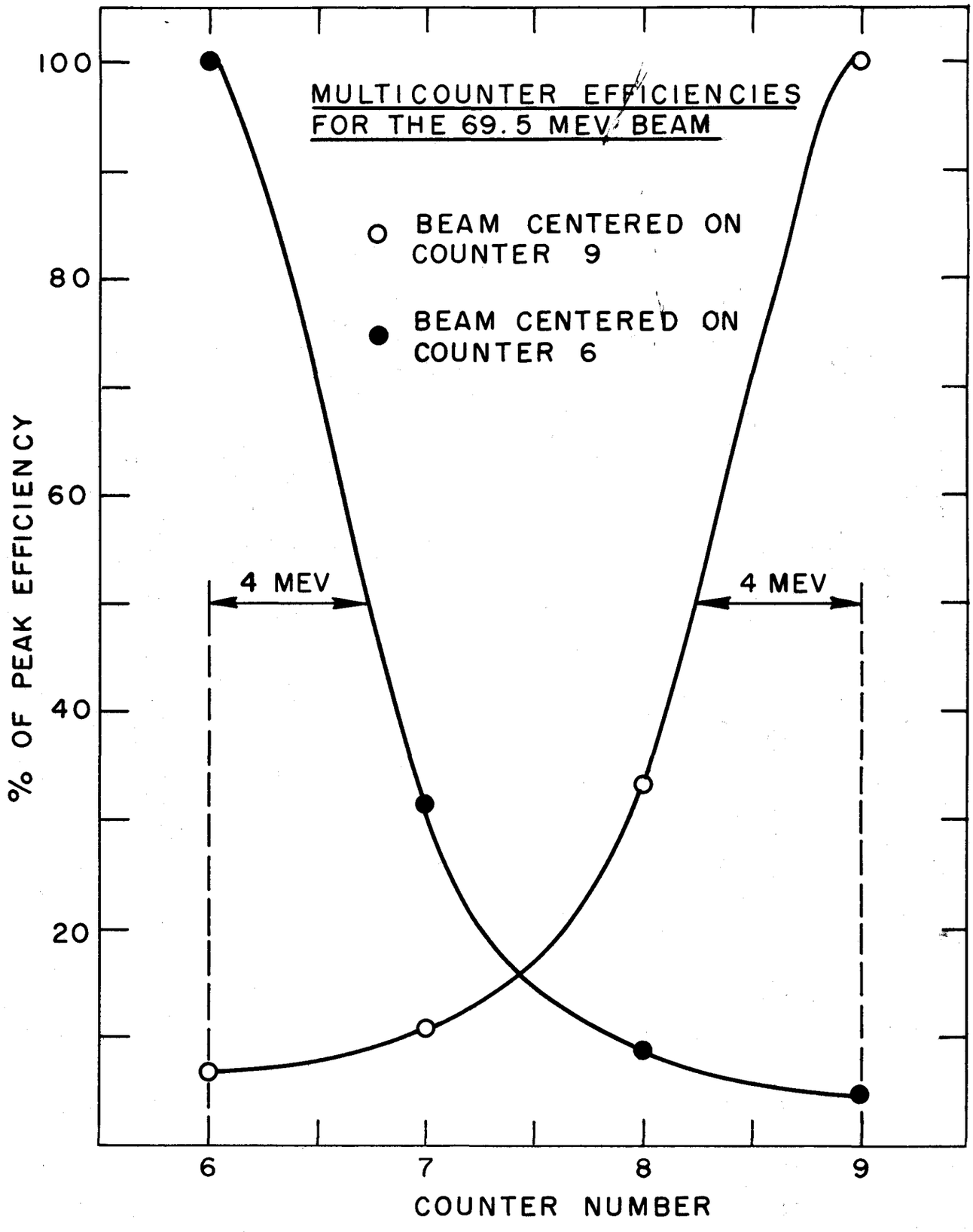
MULTICOUNTER EFFICIENCIES
FOR THE 69.5 MEV BEAM
BEAM CENTERED ON COUNTER 9
BEAM CENTERED ON COUNTER 6
4 MEV
4 MEV
% OF PEAK EFFICIENCY
100
80
60
40
20
6
7
8
9
COUNTER NUMBER

FIG. 3A

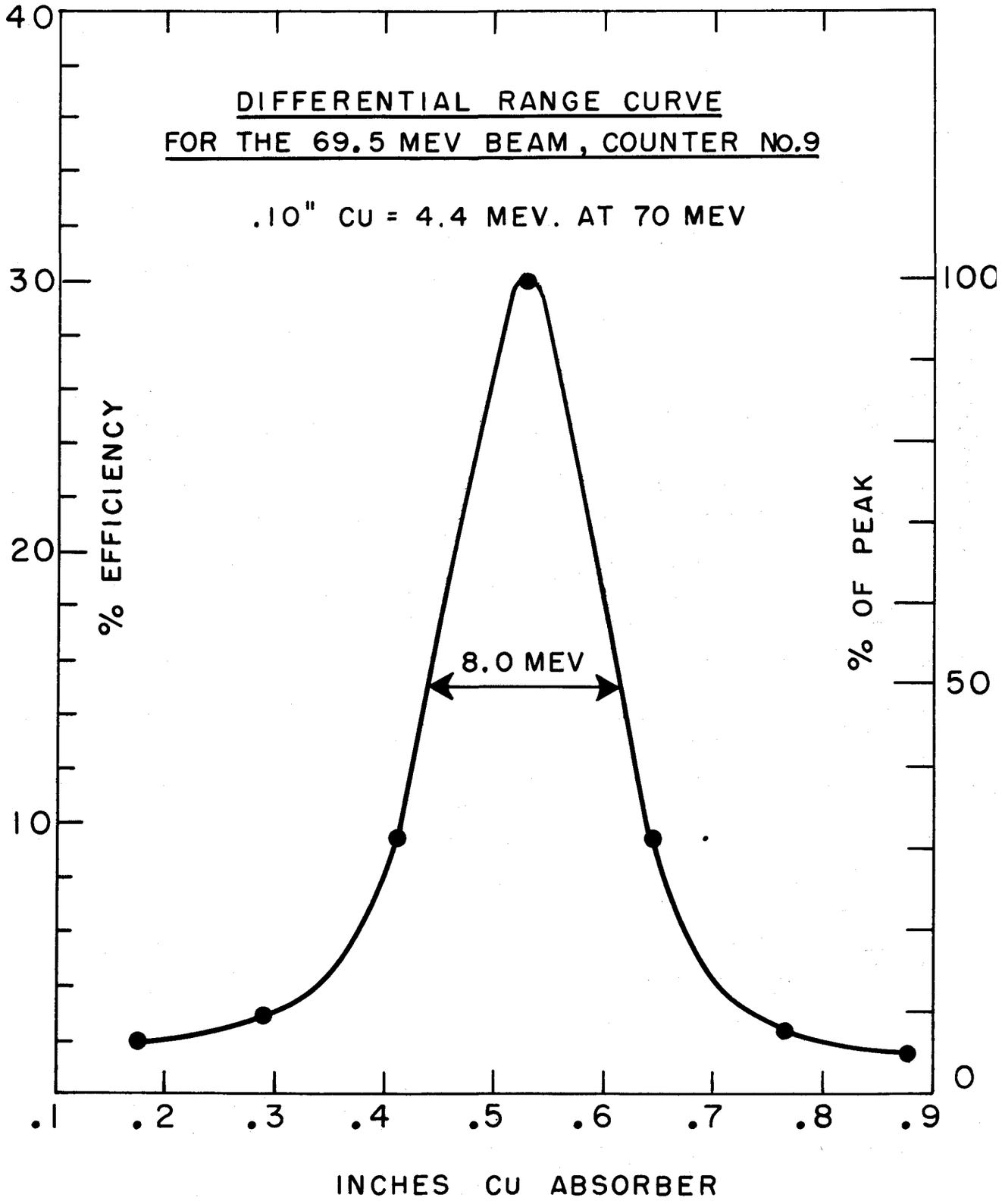
DIFFERENTIAL RANGE CURVE
FOR THE 69.5 MEV BEAM, COUNTER NO.9
.10" CU = 4.4 MEV. AT 70 MEV
40
30
20
10
% EFFICIENCY
100
50
0
% OF PEAK
8.0 MEV
.1
.2
.3
.4
.5
.6
.7
.8
.9
INCHES CU ABSORBER

FIG. 3B

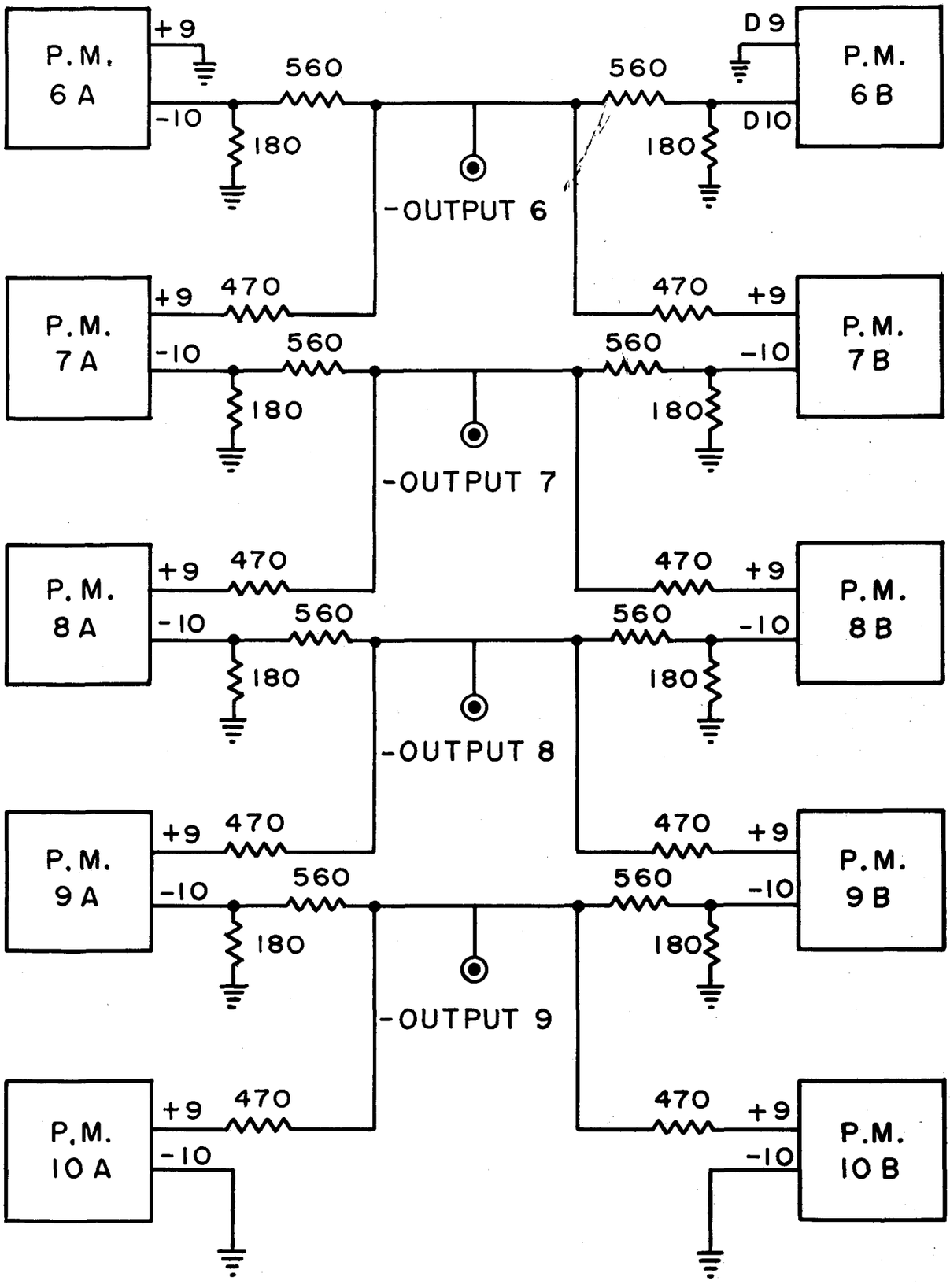

MULTICOUNTER OUTPUT CIRCUIT

FIG. 4

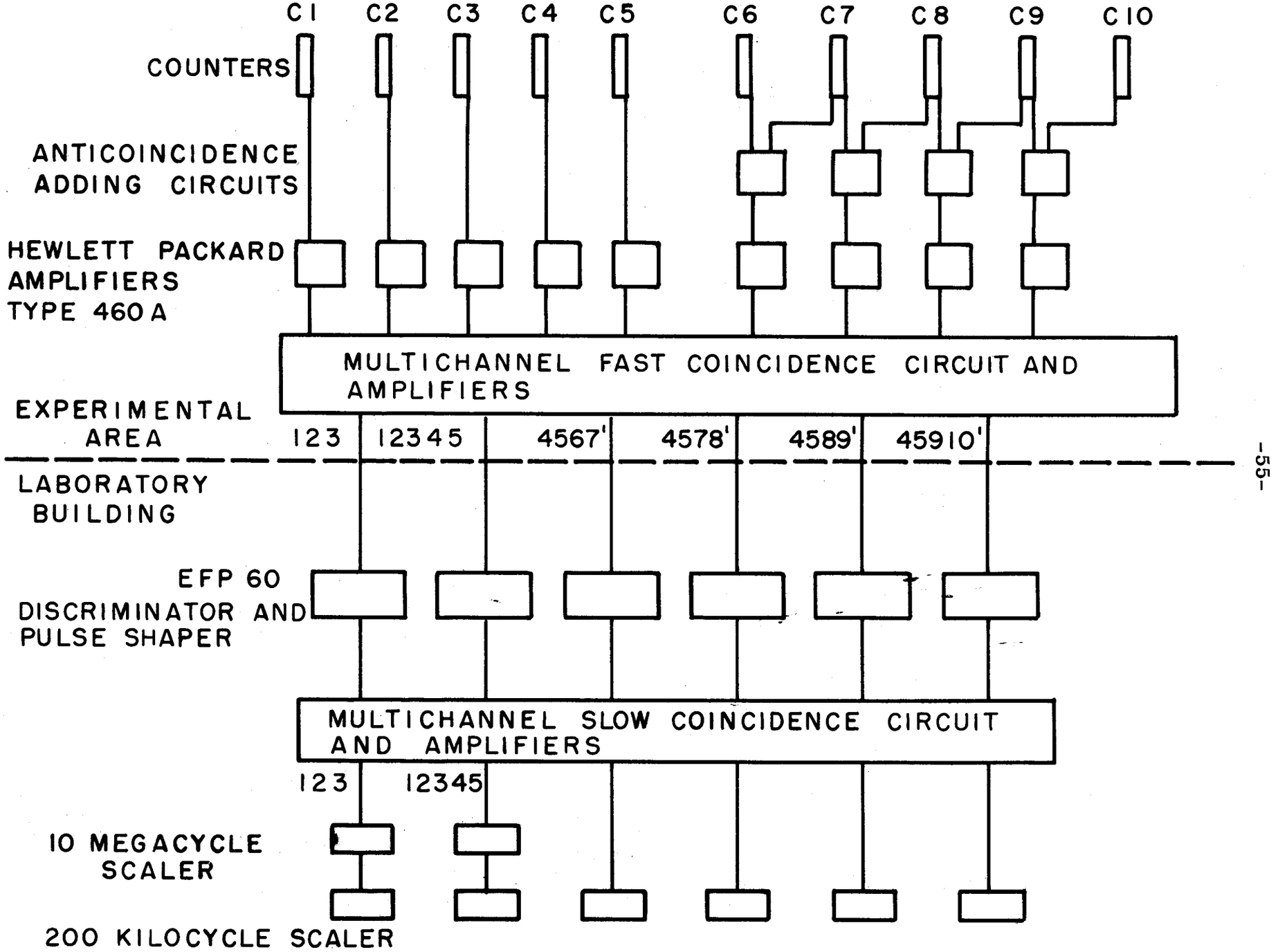

BLOCK DIAGRAM OF ELECTRONICS

FIG. 5

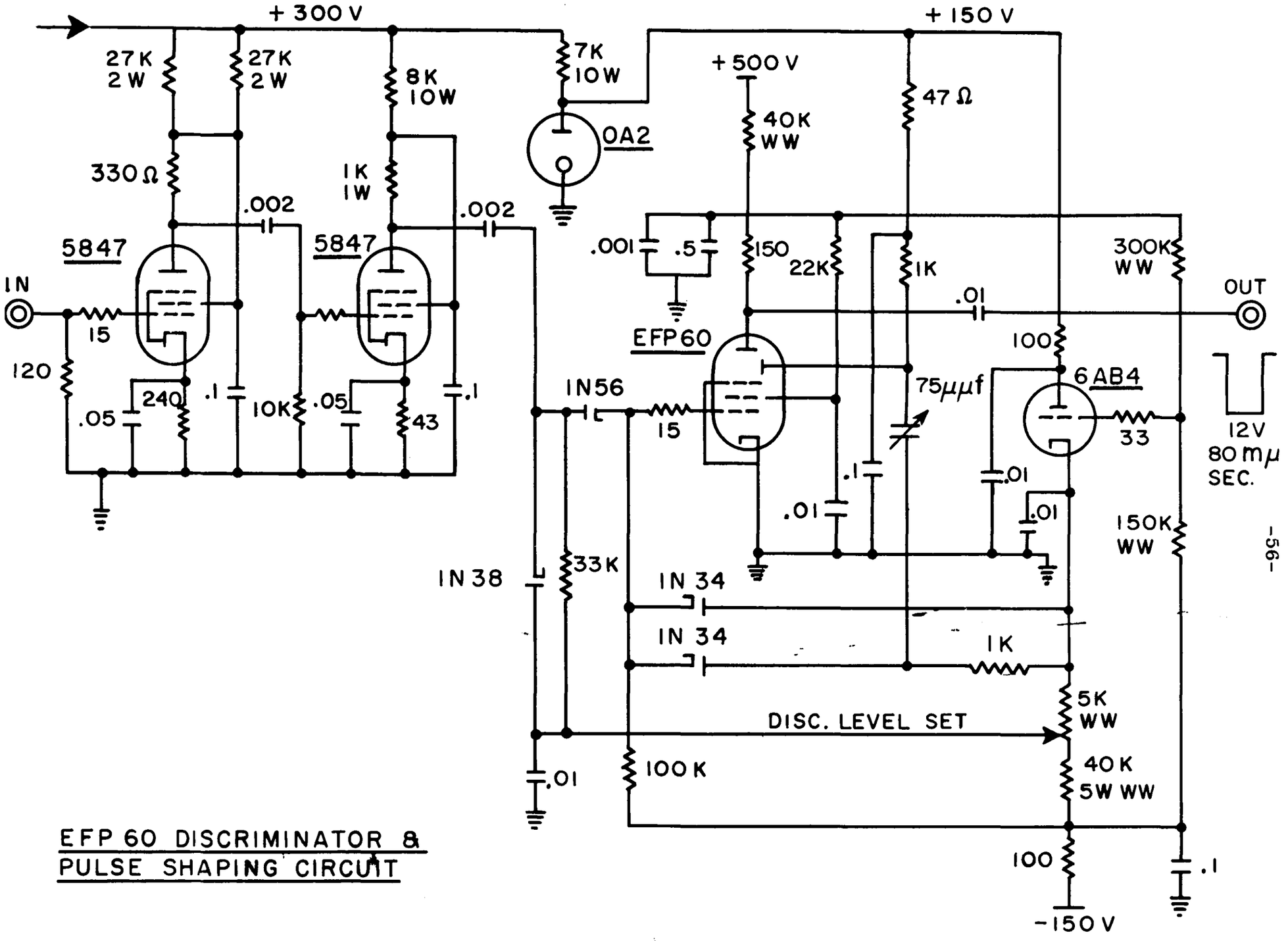

EFP 60 DISCRIMINATOR & PULSE SHAPING CIRCUIT

FIG. 6

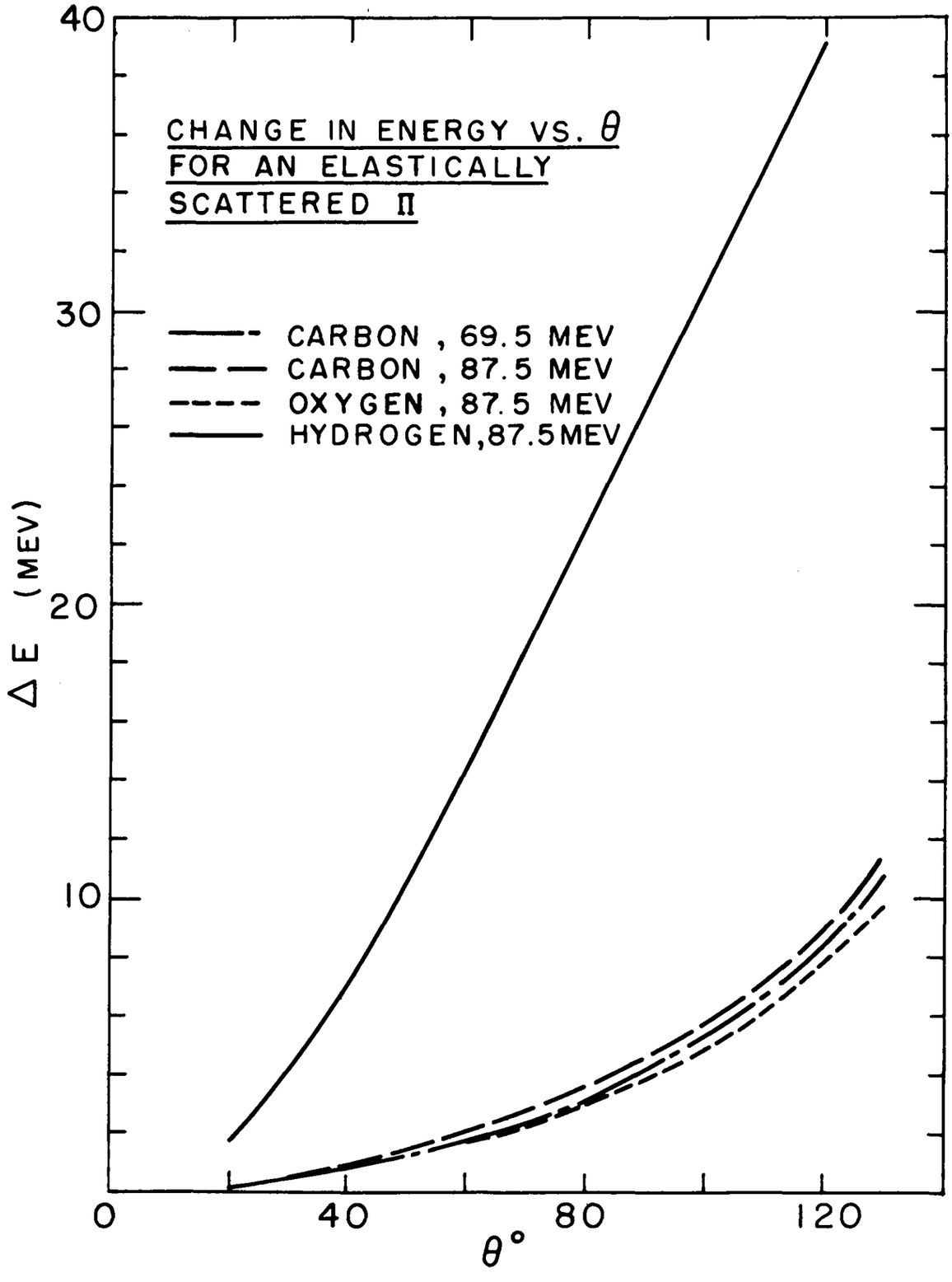
CHANGE IN ENERGY VS. θ
FOR AN ELASTICALLY
SCATTERED Π
CARBON , 69.5 MEV
CARBON , 87.5 MEV
OXYGEN , 87.5 MEV
HYDROGEN,87.5MEV
ΔE (MEV)
θ°
0
40
80
120
10
20
30
40

FIG. 7

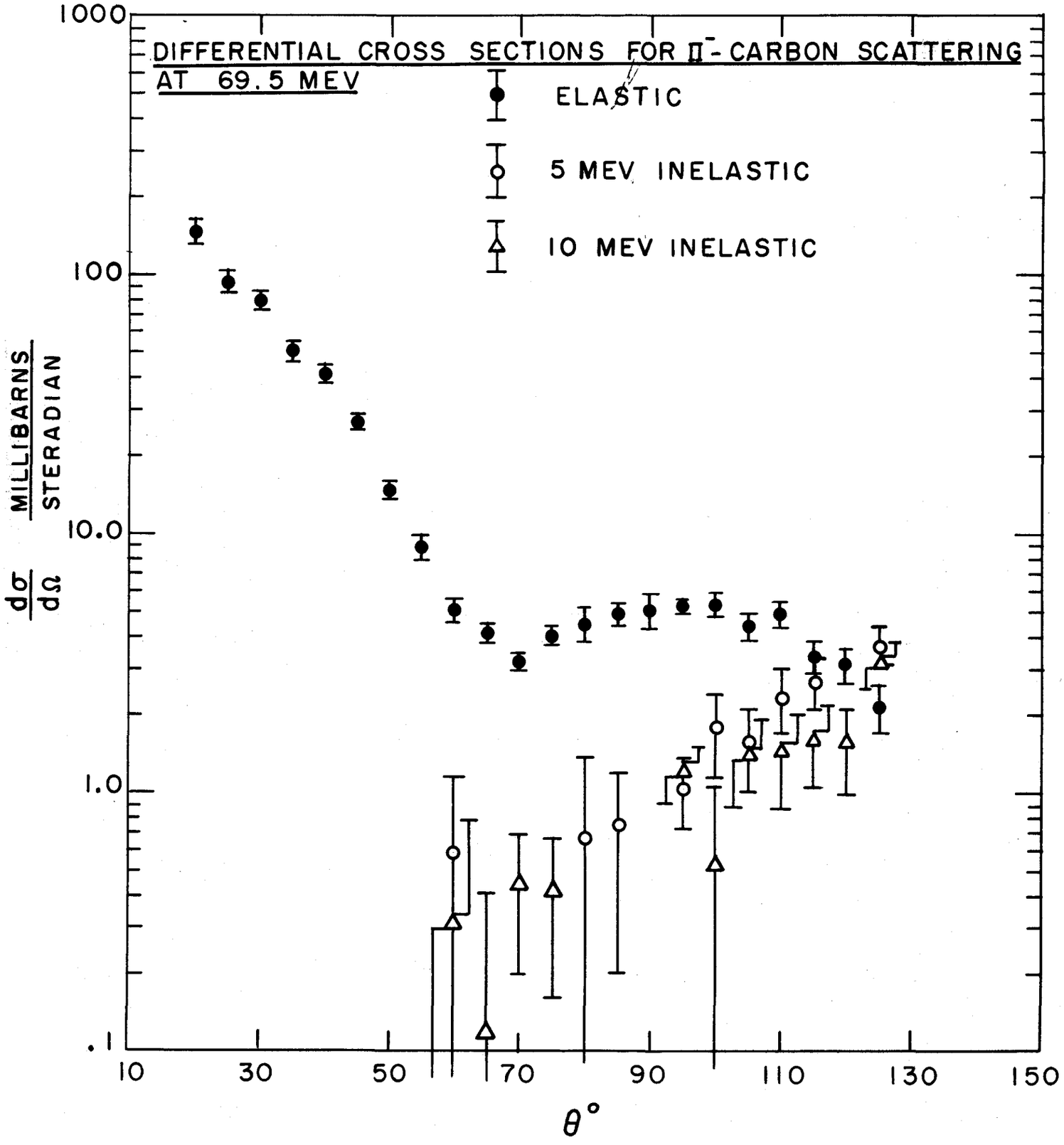
DIFFERENTIAL CROSS SECTIONS FOR π⁻ - CARBON SCATTERING
AT 69.5 MEV
ELASTIC
5 MEV INELASTIC
10 MEV INELASTIC
1000
100
10.0
1.0
.1
dσ/dΩ MILLIBARNS/STERADIAN
10
30
50
70
90
110
130
150
θ°

FIG. 8

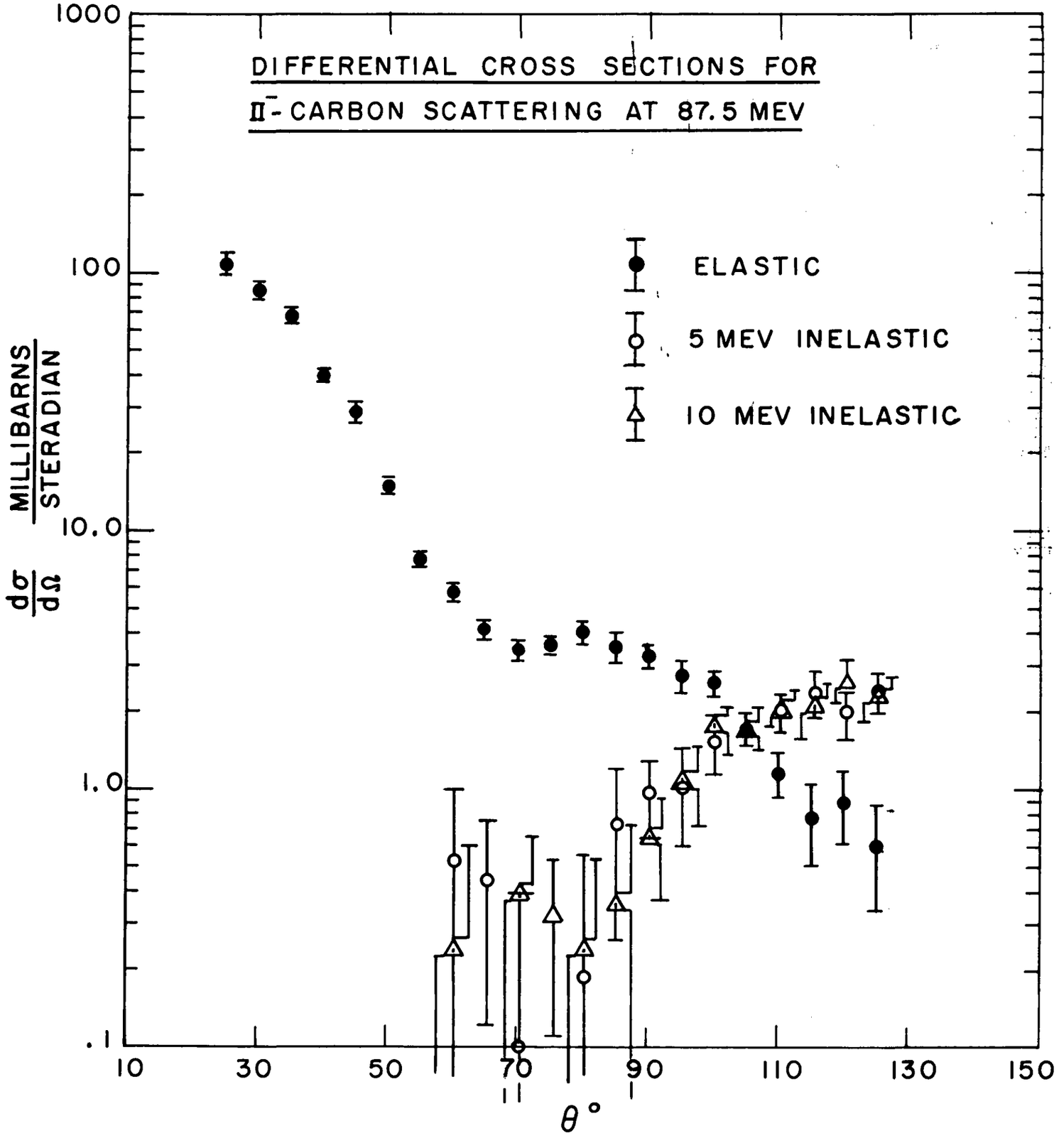
DIFFERENTIAL CROSS SECTIONS FOR
Π⁻ - CARBON SCATTERING AT 87.5 MEV
ELASTIC
5 MEV INELASTIC
10 MEV INELASTIC
dσ/dΩ MILLIBARNS/STERADIAN
1000
100
10.0
1.0
.1
10
30
50
70
90
110
130
150
θ°

FIG. 9

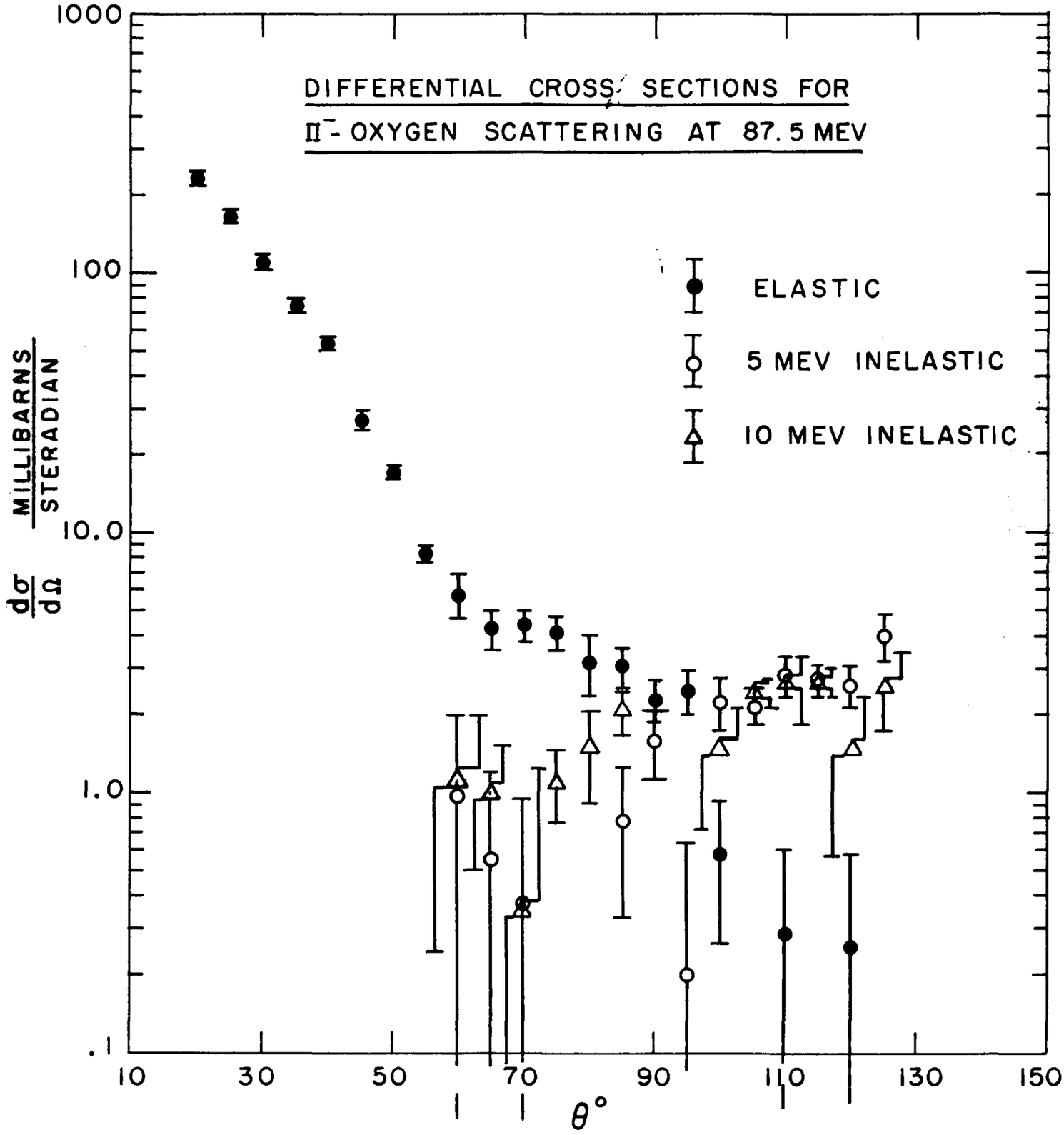
DIFFERENTIAL CROSS SECTIONS FOR
π⁻ - OXYGEN SCATTERING AT 87.5 MEV
ELASTIC
5 MEV INELASTIC
10 MEV INELASTIC
dσ/dΩ MILLIBARNS/STERADIAN
1000
100
10.0
1.0
.1
10
30
50
70
90
110
130
150
θ°

FIG. 10

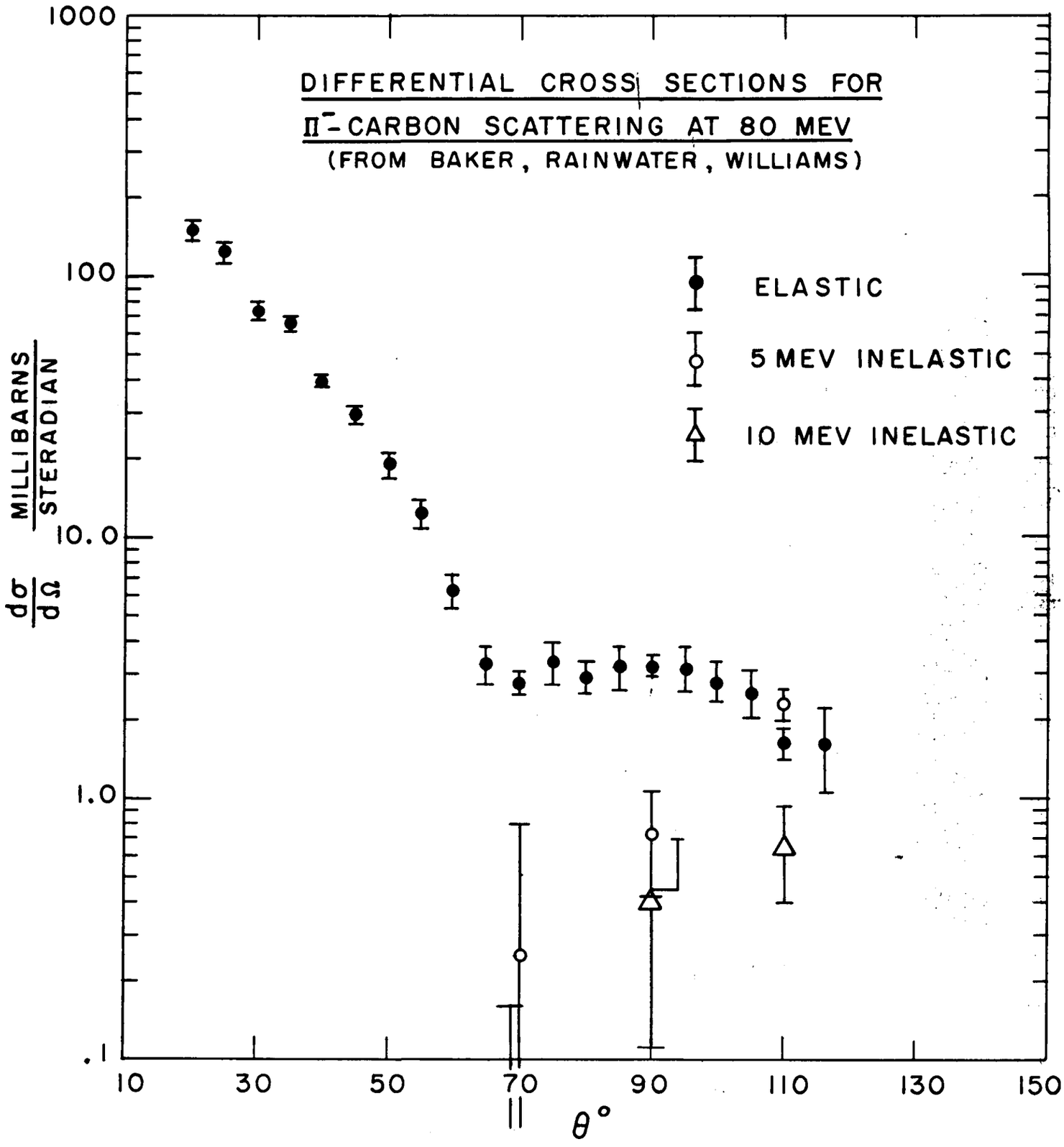
DIFFERENTIAL CROSS SECTIONS FOR
Π⁻-CARBON SCATTERING AT 80 MEV
(FROM BAKER, RAINWATER, WILLIAMS)
ELASTIC
5 MEV INELASTIC
10 MEV INELASTIC
dσ/dΩ MILLIBARNS/STERADIAN
1000
100
10.0
1.0
.1
10
30
50
70
90
110
130
150
θ°

FIG. 11

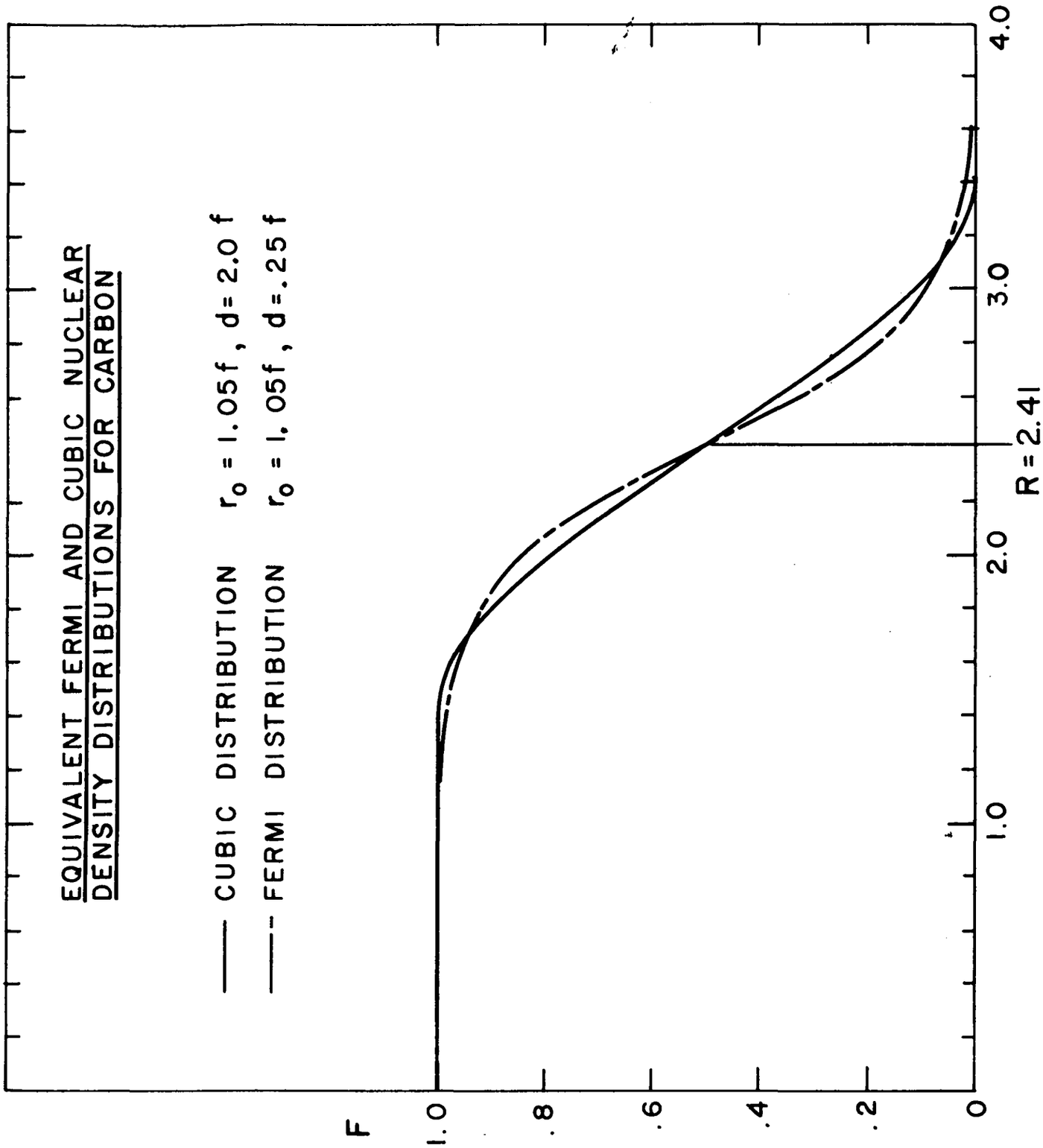
EQUIVALENT FERMI AND CUBIC NUCLEAR
DENSITY DISTRIBUTIONS FOR CARBON
CUBIC DISTRIBUTION r_o = 1.05f, d= 2.0 f
FERMI DISTRIBUTION r_o = 1.05f, d=.25 f
F
1.0
.8
.6
.4
.2
0
1.0
2.0
3.0
4.0
R=2.41
r (fermis)

FIG. 12

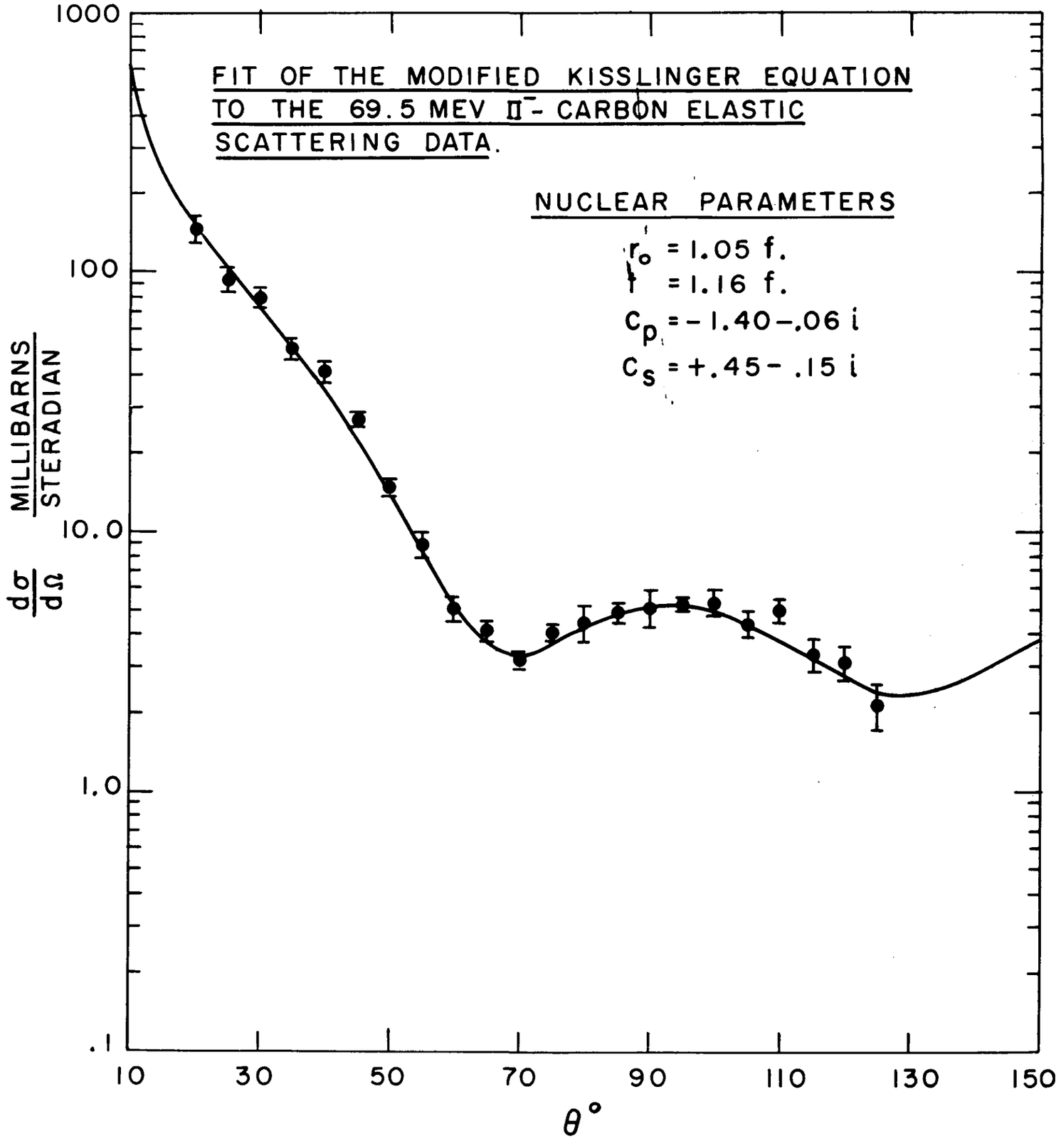
FIT OF THE MODIFIED KISSLINGER EQUATION TO THE 69.5 MEV π⁻ - CARBON ELASTIC SCATTERING DATA.
NUCLEAR PARAMETERS
r_o = 1.05 f.
t = 1.16 f.
C_p = -1.40 - .06 i
C_s = +.45 - .15 i
$\frac{d\sigma}{d\Omega}$ MILLIBARNS/STERADIAN
1000
100
10.0
1.0
.1
10
30
50
70
90
110
130
150
θ°

FIG. 13

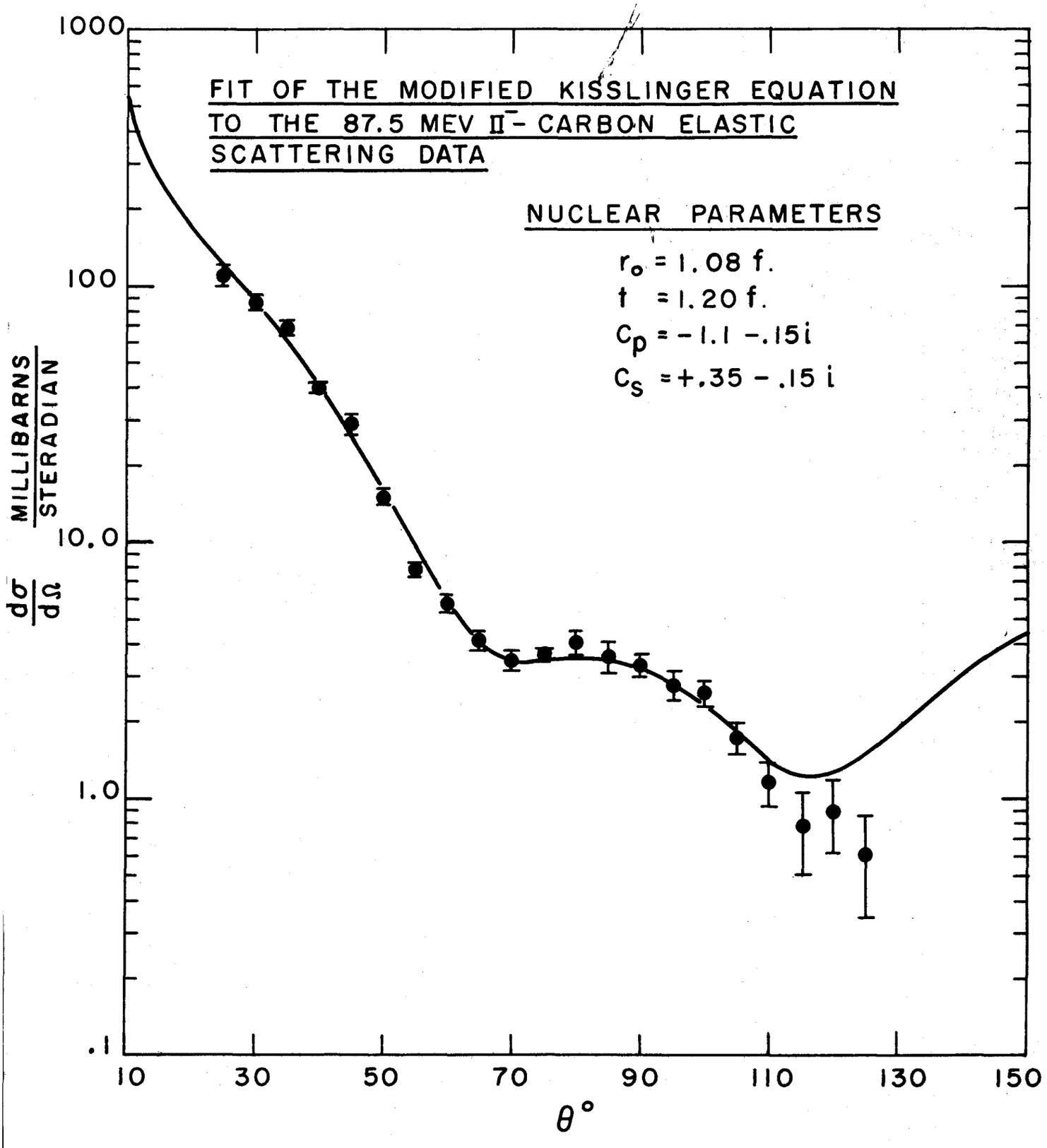
FIT OF THE MODIFIED KISSLINGER EQUATION TO THE 87.5 MEV Π⁻ - CARBON ELASTIC SCATTERING DATA
NUCLEAR PARAMETERS
r_o = 1.08 f.
t = 1.20 f.
C_p = -1.1 -.15i
C_s = +.35 - .15 i
$\frac{d\sigma}{d\Omega}$ MILLIBARNS/STERADIAN
1000
100
10.0
1.0
.1
10
30
50
70
90
110
130
150
θ°

FIG. 14

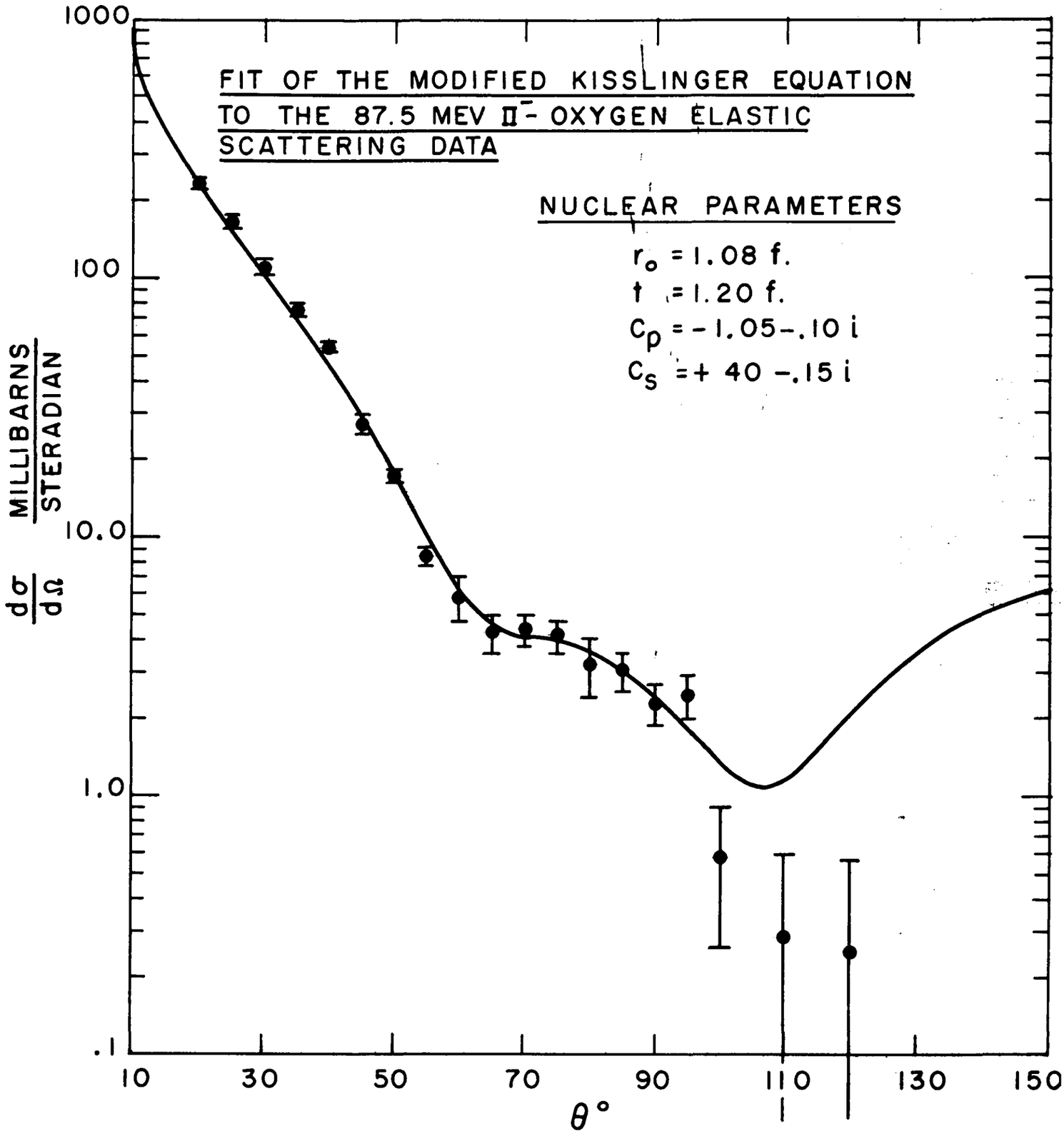
FIT OF THE MODIFIED KISSLINGER EQUATION
TO THE 87.5 MEV π⁻ - OXYGEN ELASTIC
SCATTERING DATA
NUCLEAR PARAMETERS
r_o = 1.08 f.
t = 1.20 f.
C_p = -1.05-.10 i
C_s = + 40 -.15 i
$\frac{d\sigma}{d\Omega}$ MILLIBARNS/STERADIAN
1000
100
10.0
1.0
.1
10
30
50
70
90
110
130
150
θ°

FIG. 15

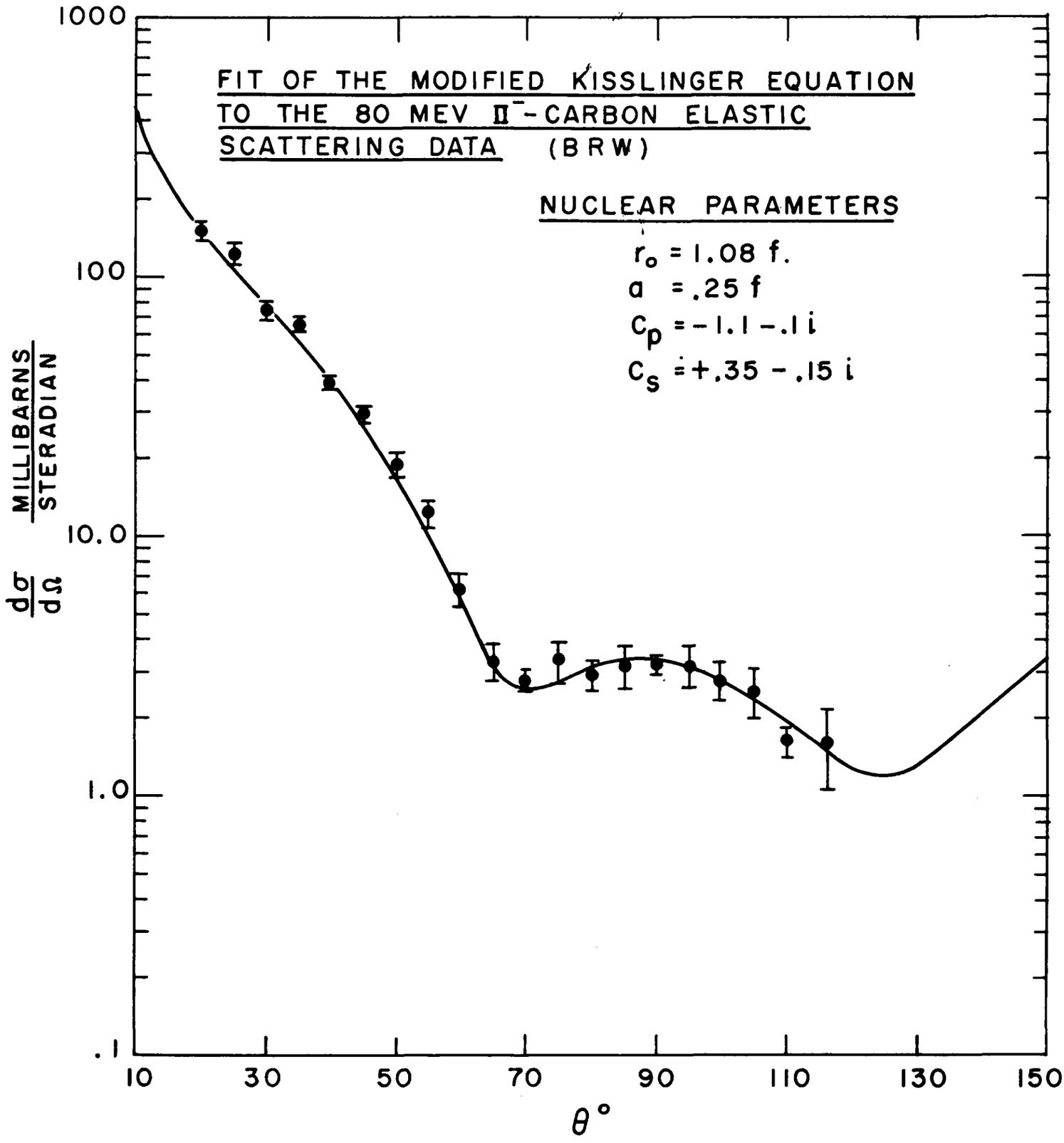
FIT OF THE MODIFIED KISSLINGER EQUATION
TO THE 80 MEV Π⁻-CARBON ELASTIC
SCATTERING DATA (BRW)
NUCLEAR PARAMETERS
r_o = 1.08 f.
a = .25 f
C_p = -1.1 -.1 i
C_s = +.35 - .15 i
$\frac{d\sigma}{d\Omega}$ MILLIBARNS/STERADIAN
1000
100
10.0
1.0
.1
10
30
50
70
90
110
130
150
θ°

FIG. 16

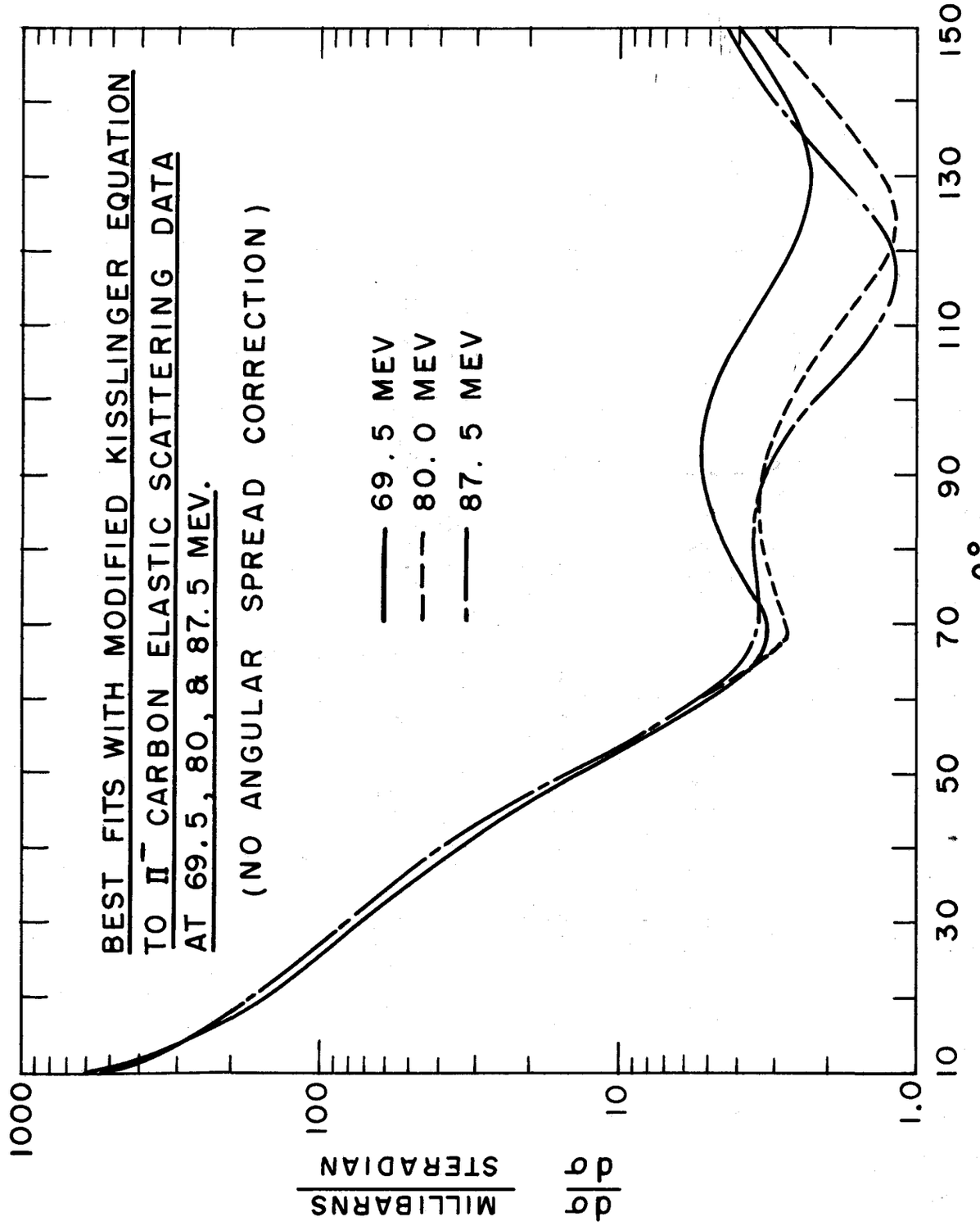
BEST FITS WITH MODIFIED KISSLINGER EQUATION
TO π^- CARBON ELASTIC SCATTERING DATA
AT 69.5, 80, & 87.5 MEV.
(NO ANGULAR SPREAD CORRECTION)
69.5 MEV
80.0 MEV
87.5 MEV
1000
100
10
1.0
10
30
50
70
90
110
130
150
$\theta°$
$\frac{d\sigma}{d\Omega}$ MILLIBARNS / STERADIAN

FIG. 17

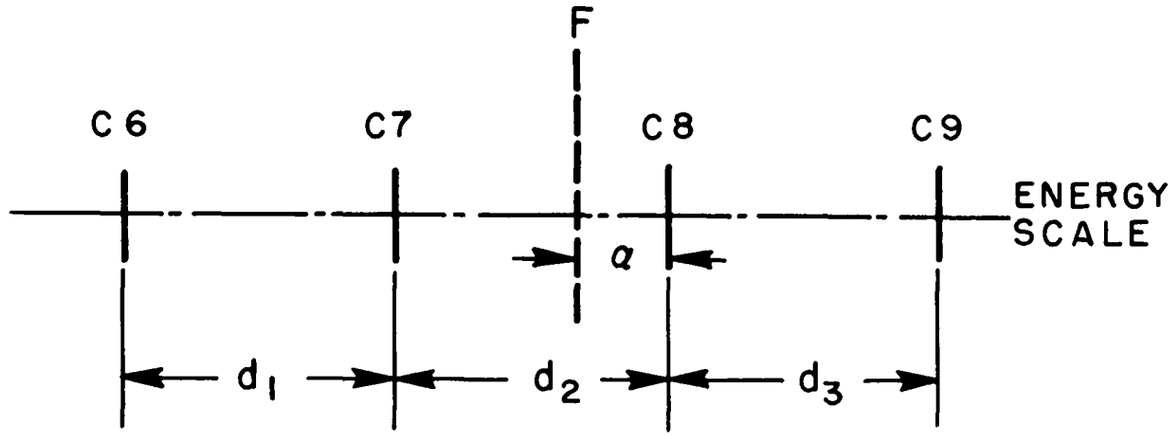

ENERGY SPACING OF COUNTERS,

MEAN ENERGIES FOR MULTICOUNTER, AND BEAM F

FIG A I